Materials Advances

ROYAL SOCIETY OF CHEMISTRY

PAPER

View Article Online
View Journal | View Issue

Cite this: *Mater. Adv.*, 2024, 5, 9292

Unveiling the synergistic effect of an nZVI–SiO_2–TiO_2 nanocomposite for the remediation of dye contaminated wastewater†

Murtala Namakka, *[ab] Md Rezaur Rahman, *[a] Khairul Anwar Mohamad Bin Said,[a] King Kuok Kuok,[c] Fahmi Asyadi Md Yusof,[d] Muneera S. M. Al-Saleem,[e] Jehan Y. Al-Humaidi [e] and Mohammed M. Rahman [f]

Water contamination and scarcity pose critical global challenges. Existing water remediation technologies such as membrane technologies lack hydrophilic surface properties, prompting the need for novel, highly efficient supportive materials. Photocatalysis emerges as a promising solution for degrading organic pollutants in wastewater. However, existing photocatalysts such as titanium dioxide (TiO_2) suffer from rapid recombination of photogenerated charge carriers and lower catalytic activity, hindering performance. Herein, a novel, high sorption capacity nZVI–SiO_2–TiO_2 nanocomposite material was synthesized *via* a combined chemical reduction approach. The influence of synthesis pH and the synergistic effects of nZVI, SiO_2, and TiO_2 on the physicochemical properties and overall performance of the nZVI–SiO_2–TiO_2 nanocomposite were investigated. Three sets of nZVI–SiO_2–TiO_2 nanocomposites were synthesized by varying synthesis pH from 2 to 4. MB dye degradation experiments and thermal analysis revealed that the nZVI–SiO_2–TiO_2 nanocomposite synthesized under pH 2 synthesis conditions exhibited the fastest dye degradation rate, highest removal efficiency (100%), and thermal stability. Characterization techniques, including FTIR, EDS (energy dispersive X-ray spectroscopy), SEM, BET (Brunauer–Emmett–Teller), XRD, TGA (thermogravimetric analysis), and DSC (differential scanning calorimetry), revealed that lower nZVI–SiO_2–TiO_2 synthesis pH enhanced the material's specific surface area, crystallinity, and the interfacial interactions of nZVI, SiO_2, and TiO_2 components in the nanocomposite. The reusability test showed >90% efficiency after 5 successive cycles. The sorption mechanism and methylene blue (MB) dye speciation test corroborated the synergistic adsorption and reduction potential of nZVI–SiO_2–TiO_2 functional materials with 100% mineralized methylene blue (MB^+ species) at MB dye solution pH above 6.0. After economic considerations, it is believed that the exceptional adsorption and recycling abilities of the novel nZVI–SiO_2–TiO_2 material, coupled with its thermal stability, could counterbalance its upfront expenses, potentially making it a feasible choice for wastewater treatment applications.

Received 26th August 2024,
Accepted 19th October 2024

DOI: 10.1039/d4ma00853g

rsc.li/materials-advances

1. Introduction

Globally, textile industries are projected to grow at a compound annual growth rate of 4.4% from 2020 to 2025, driven by increasing consumer demand and urbanization, particularly in developing economies.[1] This anticipated expansion will inadvertently exacerbate the environmental challenges posed by industrial wastewater discharge.[2] Synthetic dyes utilized in textile, plastic, and paper industries pose a major concern due to their widespread applications and high potential toxicity, as over 200 000 tons of dye are lost to effluents during textile product production cycles alone.[3–5] A plethora of these dyes and their accompanying toxic chemicals discharged into water bodies are carcinogenic and nonbiodegradable with significant

[a] *Department of Chemical Engineering and Energy Sustainability, Faculty of Engineering, University Malaysia Sarawak, Kota Samarahan, 94300, Malaysia. E-mail: namakkamurtala@gmail.com, rmrezaur@unimas.my*
[b] *Ahmadu Bello University, Zaria, Kaduna State, Nigeria*
[c] *Faculty of Engineering, Computing and Science, Swinburne University of Technology, Sarawak Campus, Malaysia*
[d] *Institute of Chemical and Bio-engineering Technology, Universiti Kuala Lumpur Malaysian (UniKl Micet), Malaysia*
[e] *Department of Chemistry, Science College, Princess Nourah Bint Abdulrahman University, P.O. Box 84428, Riyadh 11671, Saudi Arabia*
[f] *Center of Excellence for Advanced Materials Research (CEAMR) & Chemistry Department, Faculty of Science, King Abdulaziz University, Jeddah 21589, Saudi Arabia*

† Electronic supplementary information (ESI) available. See DOI: 10.1039/d4ma00853g

detrimental impacts on humans and aquatic ecosystems.[4] In 2023, the UN water conference report revealed that over two billion people (26% of the global population) lack safe drinking water, making the removal of harmful organic and inorganic contaminants discharged in water and soil environments a critical global issue threatening both public health and environmental sustainability.[6]

To address this contemporary challenge, it is crucial to develop efficient and cost-effective remediation technologies capable of combating the diverse range of toxic wastewater effluents.[4] Conventional treatment methods such as flocculation,[7,8] combination of flocculation and coagulation,[9,10] sedimentation, membrane technologies[11,12] as well as the use of trickling filters[13,14] have been utilized for decades. However, these methods lack the ability to degrade recalcitrant dyes and generate secondary waste streams.[1] Consequently, advanced oxidation processes (AOPs) and biological wastewater treatment approaches were recently explored for improved selectivity and adsorption capacity.[15,16] Conversely, long residence time for effective treatment,[17] large sludge generation,[18] and environmental concerns are the greatest challenges in these approaches.[19,20] Thus, adsorption technologies, utilizing adsorbents for environmental remediation, were reinvigorated. Adsorption emerges as a prospective alternative to conventional wastewater treatment technologies due to its simple technological requisites,[21] cost-effectiveness, and high removal efficiency for diverse contaminants coupled with limited generation of secondary pollutants.[22] Consequently, the development of efficient, cost effective, and advanced adsorbent materials is essential for practical integration of adsorption technologies in mitigating the contemporary environmental impacts of dye-contaminated wastewater. Individual and synergistically combined nanoadsorbents such as nano-zero-valent iron (nZVI),[23] silica (SiO_2),[24] titania (TiO_2)[25–27] and other composite adsorbents[28] have shown great potential for environmental and wastewater remediation operations. Recently, Das *et al.* synthesized and evaluated the sorption capacity of polyaniline-based magnesium ferrite (Pan-MgF) nanocomposite for degradation of cationic brilliant green dye, and the results corroborated the formation of the Pan-MgF nanoadsorbent with 90.28% sorption capacity for brilliant green dye.[29]

Zero valent iron (ZVI) is a cost-effective and environmentally benign adsorbent recently employed in a plethora of environmental remediation operations due to its simultaneous and synergistic adsorption and reduction capabilities.[30–34] Nano-zero valent iron (nZVI), characterized by its excellent chemical reactivity and injectivity in aquifer systems, is considered a large surface area electron donor that chemically reduces pollutants to a less harmful precipitate.[35] Despite these outstanding properties of nZVI materials in environmental remediation applications, limiting factors such as rapid passivation and particle agglomeration hindering its dispersibility and overall performance need to be addressed. Coincidently, researchers have investigated the incorporation of nZVI with other functional materials such as chitosan (CS), silica (SiO_2), and titanium dioxide (TiO_2), utilizing their synergistic effects, to overcome the susceptibility of nZVI materials to rapid oxidation and improve overall performance. For example, Zhang *et al.* (2019) synthesized a chitosan (CS) composite loaded with well-dispersed nanoscale zero-valent iron (NZVI/CS). Characterizations showed that the NZVI/CS composite contained numerous dispersed Fe^0 nanoparticles, and the NZVI/CS composite exhibited synergistic adsorption and reduction capabilities.[36] Duan *et al.* encapsulated nZVI in a porous glutaraldehyde-crosslinked chitosan (GCS), and the nZVI/GCS material showed great reusability performance.[37] Despite these advances, the stability and synergistic performance of the nZVI supported nanocomposite depend on the nature and properties of the supporting materials, making the selection of suitable supporting materials highly crucial.

SiO_2 is known for its excellent adsorption properties and ability to stabilize nZVI,[38] while TiO_2 is a widely studied adsorbent capable of mineralizing organic pollutants.[39] Previous studies have explored the use of SiO_2-supported nZVI composite materials for wastewater treatment and their results demonstrated improved performance compared to individual components.[38,40] Hejri *et al.* reported excellent nitrate removal efficiency exhibited by the TiO_2/nZVI nanocomposite with a maximum removal capacity of 98.226% achieved under optimized reaction conditions, 150 minute contact time and 4.185 pH of the solution.[39] In another study, Zhao *et al.* embedded zero-valent iron nanoparticles (nZVI) within a TiO_2 matrix *via* a one-step electrospinning process and investigated the performance of nZVI–TiO_2 nanofibers toward uranium removal. The nZVI–TiO_2 nanofibers exhibited excellent performance with significant magnetic properties due to the synergistic effects of nZVI and TiO_2 nanomaterials. Despites this synergistic performance, existing materials and their synthesis approaches often suffer from a plethora of limitations such as rapid recombination, low reducing capacity, complex operation, and the generation of secondary pollutants.

Encapsulating zero valent iron materials in SiO_2–TiO_2 functional materials *via* a combined chemical reduction method could improve chemical reactivity and catalytic activity, and slow down rapid passivation of nZVI materials.[41–46] However, the development of this ternary nZVI–SiO_2–TiO_2 composite material and the investigation of pH influence in the synthesis of this novel material have not been reported. The incorporation of SiO_2 and TiO_2 with nano-zero-valent iron (nZVI) creates a unique hybrid system that combines the strong reducing capacity of nZVI, the adsorption properties of SiO_2, and the photocatalytic activity of TiO_2. This synergistic integration of different functionalities within a single composite material epitomises a novel approach and distinguishing advantage of nZVI–SiO_2–TiO_2 over other adsorbents toward enhancing the efficiency and versatility of dye removal technologies. However, the effective synthesis of nZVI-based nanocomposites depends on the synthesis conditions, specifically the reaction pH and drying conditions.[47–49] The pH of the chemical reaction can influence the surface properties, redox potential, and interfacial interactions between the nanocomposite materials, ultimately affecting both their catalytic activity and thermal stability.[23] Hence, discerning the pH-dependent dynamics in the synthesis of nZVI–SiO_2–TiO_2 nanocomposites is essential for the optimization of this novel material for environmental

remediation applications. Thus, this study utilized three different pH levels (2, 3, and 4) to synthesize an nZVI–SiO_2–TiO_2 nanocomposite with sodium borohydride as the reducing agent. The main objectives of this study are to develop a novel nZVI–SiO_2–TiO_2 nanocomposite and examine the synergistic effects of nZVI, SiO_2, and TiO_2 functional materials on the physicochemical properties of the nZVI–SiO_2–TiO_2 nanocomposite. Other investigations include the determination of the performance of the synthesized nZVI–SiO_2–TiO_2 nanocomposites through methylene blue dye degradation experiments, evaluation of synthesis pH influence on nZVI–SiO_2–TiO_2 material performance, thermal property evaluation through TGA activation analysis, reusability tests, sorption mechanism, investigation of pH influence on MB degradation through the MB dye speciation test, and the final economic considerations.

2 Experimental

2.1 Chemicals

The chemicals used in this study were of analytical grade purity. Ferric iron nonahydrate ($FeN_3O_9{\cdot}9H_2O$), ethanol, sodium hydroxide (NaOH), sodium borohydride ($NaBH_4$), pre-synthesized SiO_2 nanoparticles and TiO_2 nanoparticles were purchased from Aldrich and used as purchased without any modification. Deionized water and other solvents used were de-oxygenated by purging nitrogen (N_2) before use.

2.2 nZVI–SiO_2–TiO_2 nanocomposite synthesis method

For the synthesis of zero valent iron nanoparticles, the procedure described in ref. 50 was followed with little modification. Briefly 0.02 moles of ferric nitrate nonahydrate ($Fe(NO_3)_3{\cdot}9H_2O$) were prepared by dissolving 8.08 g of $Fe(NO_3)_3{\cdot}9H_2O$ in 30% ethanol under continuous stirring until complete dissolution. The solution pH was adjusted to 2.0 using 0.1 M sodium hydroxide and HCl solutions. Subsequently, 0.05 moles of sodium borohydride ($NaBH_4$) were prepared by dissolving 1.89 g of $NaBH_4$ in 100 mL of deionized water (DDI) (slowly dissolving $NaBH_4$ in a glass vial before transferring and filling to the 100 mL mark). The $NaBH_4$ solution was transferred into a burette and added dropwise into $Fe(NO_3)_3{\cdot}9H_2O$ solution under continuous stirring in a nitrogen-controlled atmosphere. The formation of greenish-black precipitates indicates the initial formation of zero valent iron particles (see Fig. 1). Finally, pre-synthesised SiO_2 and TiO_2 nanoparticles (1 : 1 weight, 5.0 g) were prepared according to the procedure described in ref. 51 and introduced into the completely black zero valent iron solution. The resulting mixture was vigorously stirred further for 25 minutes. The precipitates were collected in vials and washed several times using 90% ethanol to remove excess reactants and impurities before centrifuging at 40 000 rpm and room temperature for 5 minutes. Subsequently, the precipitates were dried at 60 degrees in a mini tube furnace under a nitrogen-controlled environment for 7 hours. The procedure was repeated for pH 3 and 4. SEM, EDX, FTIR, BET, TGA and DSC were conducted to corroborate the formation of the nZVI–SiO_2–TiO_2 nanocomposite. The performance of the synthesized nanocomposite in the removal of MB dye was evaluated using UV-vis analysis at different dye concentrations. Methylene blue (MB) dye was considered as a model pollutant due to its extensive industrial applications, chemical stability, and toxicity, which make it a contemporary environmental concern. The vibrant colour of MB dye allows for easy examination and quantification, facilitating accurate assessment of our nZVI–TiO_2–SiO_2 nanocomposite's performance. The reduction of

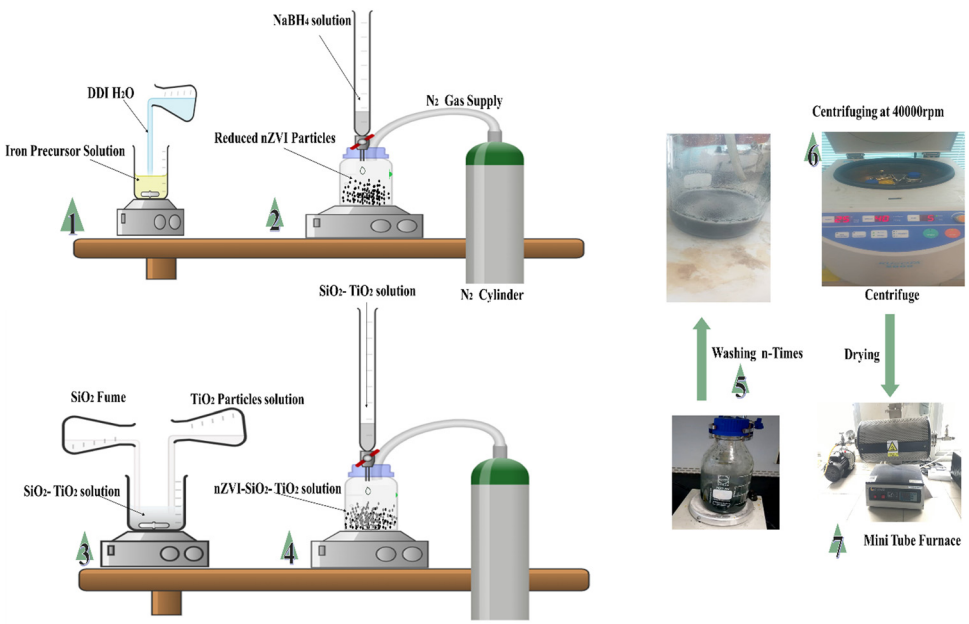

Fig. 1 Graphical representation of the nZVI–SiO_2–TiO_2 adsorbent fabrication setup.

Fe^{3+} iron to zero valent iron Fe^0 by sodium borohydride ($NaBH_4$) was governed by the following reaction:

$$2Fe(NO_3)_3{\cdot}9H_2O + 6NaBH_4 \rightarrow 2Fe + 6NaNO_3 + 3B_2H_6 + 9H_2O + 3H_2 \quad (1)$$

2.3 Characterizations and performance evaluation

The specific surface area (SSA) of nZVI–SiO_2–TiO_2 was analyzed using a BET analyser. Nitrogen adsorption–desorption isotherms were measured with a Quantachrome NovaWin2 analyser after the samples were degassed at 120 °C for eight[8] hours under nitrogen flow to remove impurities. The morphological characteristics of the synthesized nZVI–SiO_2–TiO_2 nanocomposites were examined using a Hitachi S-4700 field emission scanning electron microscope (FESEM). The samples were prepared by mounting them on aluminium stubs and applying a fine coating using a 'JFC-1600' instrument from JEOL Ltd (Japan). The FESEM images of the sample surfaces were captured using a Hitachi S-4700 FESEM with a field emission gun operating at a voltage of 20 kV. This analysis was reinforced with EDX to examine the elemental compositions of the nanocomposites. X-ray diffraction (XRD) analysis was also conducted to assess the crystallinity of the nanocomposites and identify the presence of crystalline or amorphous phases. The nanocomposite samples were examined at room temperature using a Rigaku SmartLab powder X-ray diffractometer equipped with CuKα radiation (λ = 1.5418 Å). The XRD patterns of all samples were recorded in the 2θ range of 5 to 90 degrees, with a scanning rate of 2 min^{-1}. Differential scanning calorimetry (DSC) and thermogravimetric analysis (TGA) were conducted to investigate the thermal stability and the corresponding thermal properties of the synthesized nanocomposites following the steps described in the standard procedure: at onset (323.69 °C), inflect. point (372.92 °C), end set (388.95 °C) and midpoint (351.52 °C) temperature and constant N_2 supply. Subsequently UV-vis spectroscopy was employed to analyse the performance of the nanocomposite materials in the degradation of methylene blue contaminated water. During UV-vis analysis, methylene blue solutions with three different concentrations of 3 ppm, 5 ppm, and 10 ppm were prepared from 100 ppm stock solution (using the $C_1V_I = C_2V_2$ relation). Approximately, 5 mL of each of the samples was transferred to a 10 mm length UV-vis cuvette and subsequently analysed using a UV-vis spectrophotometer in the wavelength range of 500–700 nm to obtain the standard curve. Based on the standard curve, the UV-vis sample analysis was conducted using baseline parameters in the wavelength range of 660 to 670 nm. 0.1 g L^{-1} of the synthesized nZVI–SiO_2–TiO_2 nanocomposite was used at varying dye concentrations and reaction times. This performance experiment was conducted at room temperature and a fixed pH value (pH = 6.0 MB dye solution). The findings are discussed in Section 3.

3. Results and discussion

3.1 Surface morphology and elemental analysis

The nZVI–SiO_2–TiO_2 nanocomposites were synthesized through a combined chemical reduction method described in ref. 50 and 51 utilizing iron nonahydrate precursor and sodium borohydride as the reducing agent. To investigate the morphological structure and elemental composition of the synthesized nanocomposites, scanning electron microscopy–energy dispersive X-ray spectroscopy (FESEM–EDS) techniques were employed. These analytical methodologies are widely recognized as effective approaches for examining surface morphologies and identifying the elemental constituents at the microscopic scale.[4,52–57] Fig. 2 shows the morphological structures of the nanocomposites captured using a Hitachi S-4700 FESEM with a field emission gun operating at a voltage of 20 kV at different reaction pH

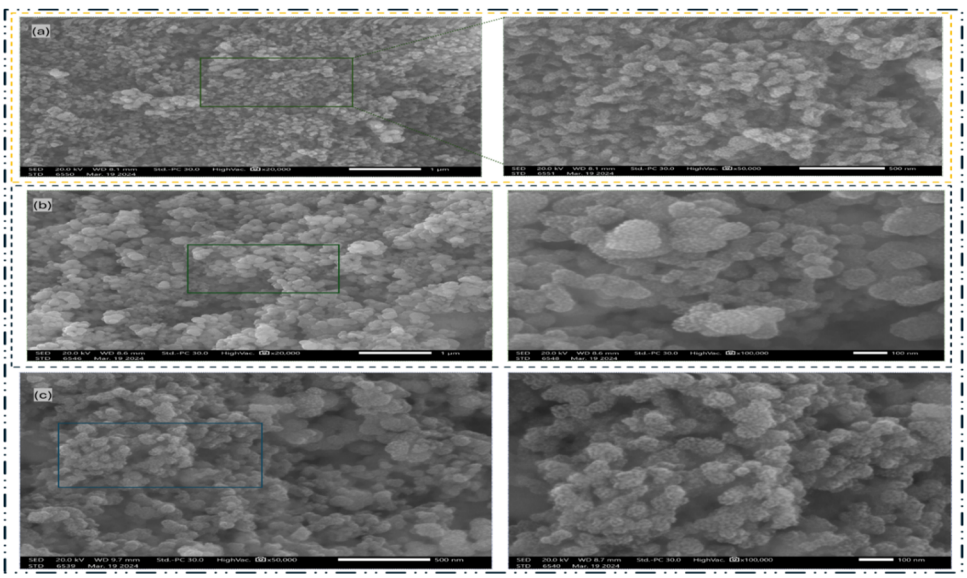

Fig. 2 FESEM images of nZVI–SiO_2–TiO_2 at different reaction pH levels: (a) pH 2 at ×20 000 and ×5000; (b) pH 3 at ×20 000 and ×100 000 and (c) pH 3 at ×5000 and ×100 000 magnifications.

levels. As shown in Fig. 2(a), at pH 2 and ×20 000 and ×50 000 magnifications, the nanocomposite displays a relatively irregular shape, with a non-uniform distribution of particles throughout the matrix, suggesting a low-level homogeneity, a characteristic property of nZVI materials.[47,51,58,59]

The presence of small sized particles within the nanocomposites observed across the pH levels corroborates the possible formation of mesopores.[60,61] Although as the synthesis pH increased from 2 to 4, the particle irregularity decreases, low level homogeneity was consistent across all pH levels. Fig. 2(a)–(c) reveals an increased particle sizes as the reaction pH increases, and this is particularly important since the sizes of nanomaterials influence their chemical reactivity and photocatalytic activity due to the availability of sufficient surface area for chemical reactions.[62,63] Subsequently, the elemental compositions of the nanocomposites were analysed through energy dispersive X-ray spectroscopy (EDS). Fig. 3 shows an increasing pattern for nZVI percentage by mass ratios in the nanocomposites, and these ratios indicate low iron oxide (FeO_x) conversion or possible precipitation at these pH levels confirming the influence of synthesis pH on nZVI conversion and their subsequent incorporation in the nanocomposite material.[64,65] It is imperative to note that interfacial interactions, redox reactions, as well as particle nucleation and growth can significantly influence the distribution and relative abundance of the nanoparticles and enhance or limit their incorporation in the nanocomposites. These factors (*viz.* interfacial interactions, redox reactions and nucleation and growth of nanoparticles) are in turn dependent on the pH of the chemical reactions.[66,67]

3.2 X-ray diffraction, BET (Brunauer–Emmett–Teller), and IR analyses

X-ray diffraction (XRD) and BET (Brunauer–Emmett–Teller) are two important characterization techniques that are commonly utilized to analyse the crystalline structures, phase compositions, pore volumes, pore size and specific surface area of nanomaterials.[4] These analytical methods are combined herein to provide a holistic view of the phase, morphologies and/or textural properties and purity. Fig. 4 shows the XRD and BET analysis results of nZVI–SiO_2–TiO_2 nanocomposites synthesized at different pH levels. Characteristic peaks observed at 48°, 53°, 63°, 54.8° and 75° in Fig. 4a are commonly assigned to the anatase, rutile and amorphous forms of SiO_2, TiO_2 and nZVI materials (see Table 1).

Consequently, the peaks observed at 37.4° and 63.7° reflected from the planes (002) and (105, 211), respectively, are assigned to the index planes of silica tetragonal rutile and titania tetragonal phases (Table 1). For the nano-zero-valent iron (nZVI) component, three characteristic diffraction peaks observed at 44.9°, 55.1°, and 75° reflected from the planes (004), (004), and (105) are assigned to amorphous Fe^0 (see Table 1). However, in the diffraction pattern of the nZVI–SiO_2–TiO_2 composite prepared under the pH = 2 condition, no significant peaks were observed aside from the three characteristic peaks assigned to amorphous Fe^0, SiO_2 and TiO_2 phases. This suggests that no new phases were formed during the chemical reduction process under this reaction condition.

The presence of hysteresis in Fig. 4(a)–(c) strongly confirmed the presence of porosity in the nZVI–SiO_2–TiO_2 nanocomposite material. The hysteresis loop with a closed ended cylindrical

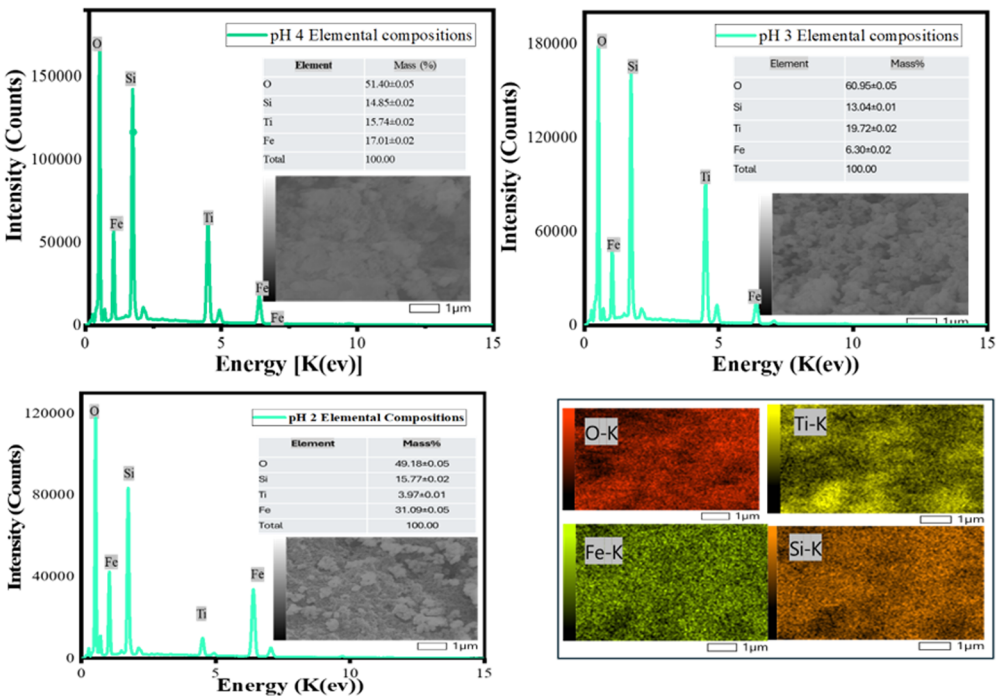

Fig. 3 Energy dispersive X-ray spectroscopy (EDS) of nZVI–SiO_2–TiO_2 synthesized at pH 4, pH 3 and pH 2.

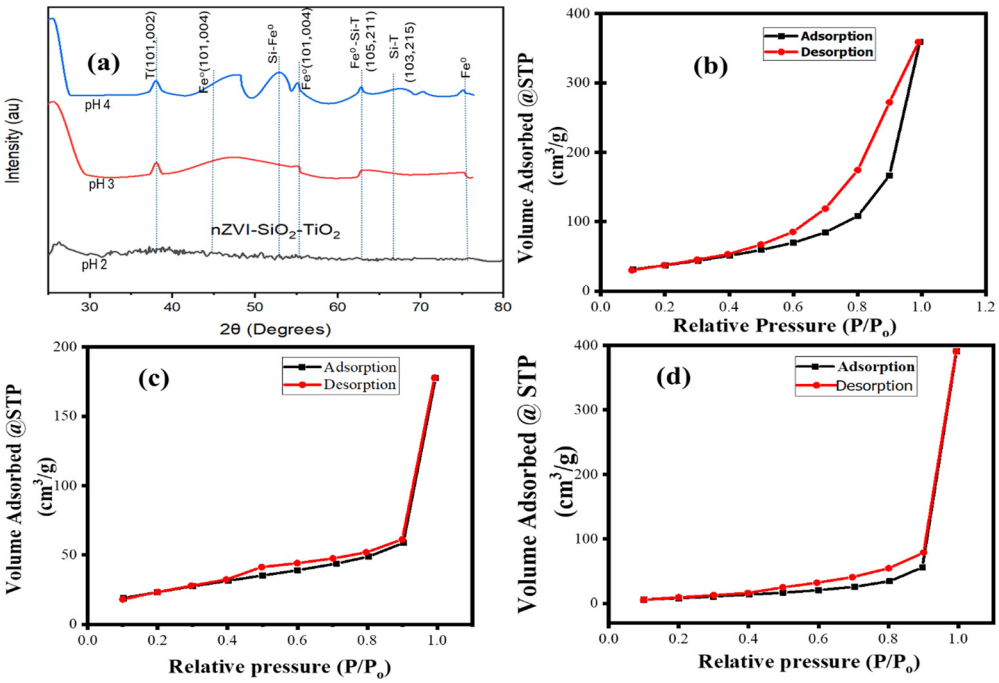

Fig. 4 XRD and BET analysis of nZVI–SiO_2–TiO_2. (a) XRD stacked plots of nZVI–SiO_2–TiO_2 at different pH levels. (b) Adsorption–desorption isotherms at pH 2. (c) and (d) Adsorption–desorption isotherms at pH 3 and pH 4, respectively.

Table 1 Identified peaks from XRD analysis of the novel nZVI–SiO_2–TiO_2 nanocomposites under different reaction conditions

SiO_2–TiO_2–nZVI	Experimental peaks	Ref.
pH 2	Ti(101), (102), (215) Fe^0(004), (101), (105) Si(105), (211), (215)	68–71
pH 3	Ti(101), (102), (215) Fe^0(004), (101), (105) Si(105), (211), (215)	68–71
pH 4	Ti(101), (102), (215) Fe^0(004), (101), (105) Si(105), (211), (215)	41 and 69–71

shape observed in Fig. 4(b) resulted from the physical processes of adsorption and desorption being relatively different. The adsorption that occurred from the side of the nZVI–SiO_2–TiO_2 inward, due to condensation, progressed until the nZVI–SiO_2–TiO_2 pores were completely filled resulting in the formation of a type IV adsorption isotherm.[72] The pore size distribution shown in Fig. 5(a) corroborated these mesoporous particles with 2–50 nm diameter distribution. A similar pattern was reported in ref. 73. The observed desorption isotherm shows a gradual slope associated to restrictions in pore entrance, a typical characteristic of type H2b hysteresis loops. From Fig. 4(b) and (c), it can be seen that the adsorption isotherm is flattened at low pressure with condensation as the relative pressure increases, while the corresponding desorption isotherms abruptly close the adsorption isotherms, indicating the occurrence of cavitation phenomena or possible bubble formation during the desorption process which is an indication of a type II adsorption isotherm with a type H3 hysteresis loop.[72] Typically, a type II isotherm with type H3 hysteresis is characterized by the presence of micro- and mesopores and this was confirmed in the pore size distribution curve (Fig. 5(b) and (c)), where the pore diameter of the particles is inclined towards the micropore region (below 2.0 nm diameter), which is more pronounced as the synthesis pH was increased from 3 to 4. As shown in Fig. 4(b) and Table 2, at pH 2 the nZVI–SiO_2–TiO_2 nanocomposite exhibited a relatively high surface area of 130.783 $m^2\ g^{-1}$, indicating a significant amount of accessible surface for adsorption and catalytic reactions.[74,75] From Table 2, in the above reaction condition, the average pore radius of 80.47939 Å suggests the presence of mesopores, which is ideal for accommodating dye molecules.[76] The total pore volume of 5.545×10^{-1} cc g^{-1} reflects the availability of sufficient pore space for dye adsorption as the pH is increased to 3, and the nZVI–SiO_2–TiO_2 nanocomposite exhibited a reduced surface area of 4.850 $m^2\ g^{-1}$ compared to pH 2. This decrease in surface area suggests probable structural changes or aggregation.[48] Furthermore, the average pore radius of 1.13346×10^3 Å indicates the presence of larger pores which can also be seen on the adsorption/desorption isotherm in Fig. 4(c). This indicates the potential formation of macro- or mesopores with a reduced total pore volume of 2.749×10^{-1} cc g^{-1}. As shown in Fig. 4(d), however, at pH 4 the nZVI–SiO_2–TiO_2 nanocomposite exhibited an intermediate surface area which is 7.8 times greater than that at pH 3. The average pore radius of 3.13847×10^2 Å suggests the presence of smaller mesopores compared to pH 2. The total pore volume of 6.050×10^{-1} cc g^{-1} indicates a relatively high availability of pore space for adsorption compared to the previous pH level.[3] These variations can influence the

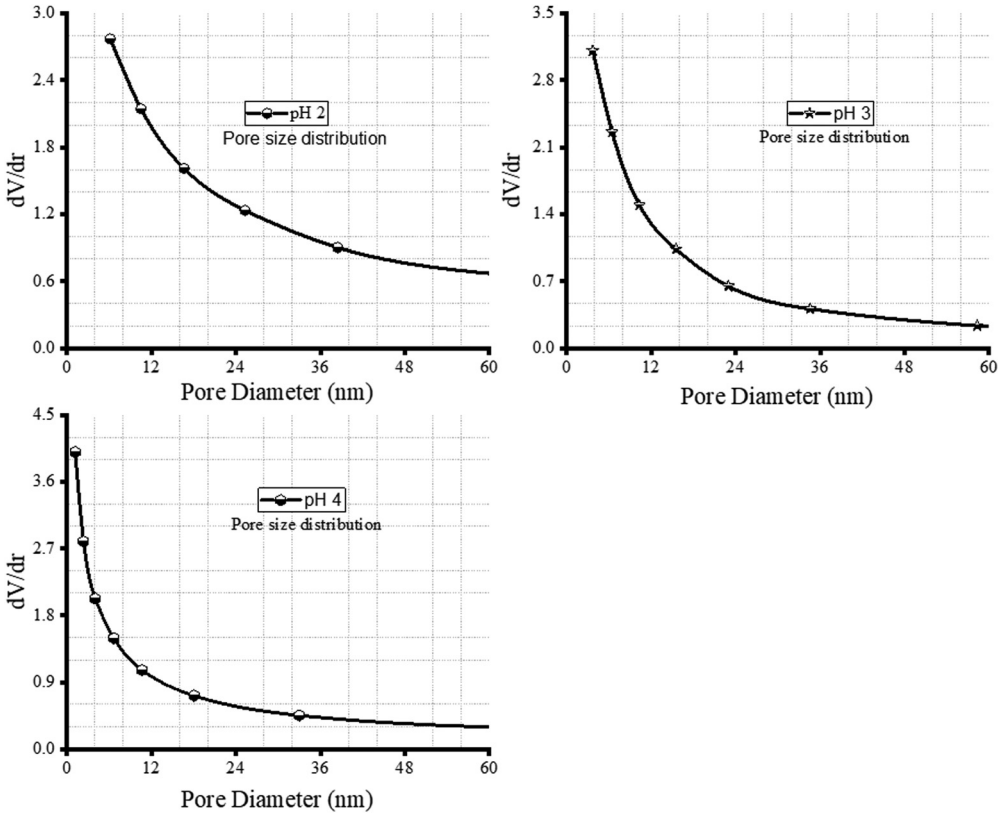

Fig. 5 Pore size distribution curves of the SiO_2–TiO_2–nZVI nanocomposite synthesized at pH 2, 3 and 4.

Table 2 BET analysis results of the SiO_2–TiO_2–nZVI nanocomposite under varying reaction conditions (pH)

SiO_2–TiO_2–nZVI	Surface area (m^2 g^{-1})	Average pore radius	Total pore volume
pH 2	130.783	80.47939 Å	5.545×10^{-1} cc g^{-1} For pores smaller than 1685.8 Å (radius) at P/P_0 = 0.9942
pH 3	4.850	1.13346×10^3 Å	2.749×10^{-1} cc g^{-1} For pores smaller than 1660.7 Å (radius) at P/P_0 = 0.9942
pH 4	38.555	3.13847×10^2 Å	6.050×10^{-1} cc g^{-1} For pores smaller than 1664.1 Å (radius) at P/P_0 = 0.9942

performance of the nanocomposite in terms of dye adsorption capacity and catalytic activity[3,77] corroborating the influence of pH variation on the fabrication, physicochemical properties, and catalytic activity of the nZVI–SiO_2–TiO_2 nanocomposite.

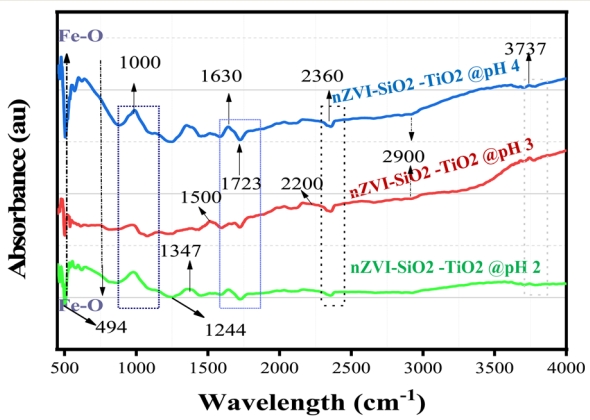

Fig. 6 FTIR analysis of nZVI–SiO_2–TiO_2 nanocomposites synthesized at different pH values (2, 3 and 4).

3.2.1 Infrared Raman (IR) spectroscopy analysis. Infrared Raman (IR) spectroscopy utilizes Raman scattering of a material subjected to irradiation by monochromatic light or a laser to obtain information on the chemical bonding properties of the material. Fig. 6 shows the FTIR spectra of nZVI–SiO_2–TiO_2 nanocomposites synthesized at pH 2 (a), pH 3 (b) and pH (4), respectively.

The vibrational bond stretching of Ti–O–Ti and Fe–O was observed in the 484–500 cm^{-1} range, and these peaks are attributed to metal–oxygen bonds which play a significant role in the adsorption support provided by TiO_2 to the nZVI component of the nZVI–SiO_2–TiO_2 nanocomposite.[78] However, overlapping peaks in this region could indicate a probable –Si–O bending vibration. Fe–O–H vibrational bond stretching peaks are indicated between 500 and 742 cm^{-1} of the absorption band,[79] while the bonding vibration between Fe–O–Ti is characterized by the absorption peak at 2360 cm^{-1}.[80] Similarly, peaks in the range from 1000 to 1006 cm^{-1} of the absorption bands are associated to the Si–O–Ti asymmetric or

Si–O–Si symmetric stretching vibrations on the surface of the nZVI–SiO_2–TiO_2 nanocomposites which in this case are observed to be negatively shifted gradually as the pH increases from 2 to 4,[81] while the peaks at 600 cm^{-1} and 1100 cm^{-1} indicate the existence and vibrational modes of the hydroxyl groups (O–H) bonded to the iron (Fe) or titanium (Ti) atoms, *i.e.* Fe–OH or Ti–OH.[82] These hydroxyl groups are a crucial part of the surface chemistry of nZVI–SiO_2–TiO_2 and can influence the adsorption, catalytic, and other functional properties of the nZVI–SiO_2–TiO_2 nanocomposite material. The peak at 1630 cm^{-1} represents –O–H bending vibrations on the nZVI surface. Comparing the spectra of nZVI–SiO_2–TiO_2 at pH 2, pH 3 and 4, it can be deduced that the overall shape and peak positions are quite similar. However, there are subtle differences in peak intensities, which might indicate variations in the surface chemistry of the nanocomposites at different pH levels, corroborating the influence of pH in the synthesis of this novel material.

3.3 Differential scanning calorimetry (DSC) and thermogravimetric analysis (TGA)

DSC and TGA are two complementary techniques that are used to investigate the thermal characteristics and properties of materials.[83,84] The DSC technique provides information about the thermal transitions and phase changes that occur within nanocomposites, such as melting, crystallization, oxidation, or decomposition events, by measuring the difference in heat flow between the sample and a reference material as a function of temperature or time.[4] The TGA technique on the other hand measures the change in the mass of a sample as a function of temperature or time to provide information about the thermal stability and decomposition behaviour of the composite materials.[4] Fig. 7 and 8 provide the DSC and TGA analysis results, and the TGA curves in Fig. 8 show the weight loss behaviour of the nanocomposite as a function of temperature. It indicates the temperature range over which the nanocomposite exhibits thermal stability, as well as the onset of decomposition or mass loss events. The varying slopes and inflection points in the TGA curves (Fig. 8(a)) suggest that the nanocomposite undergoes multiple stages of thermal decomposition or mass loss due to the release of adsorbed moisture and/or the oxidation/reduction of the inorganic phases (*e.g.*, zero-valent iron, titanium dioxide, silica). At lower temperatures (< 400 °C), the nanocomposite prepared at pH 4 shows the highest thermal stability, followed by pH 3 and pH 2. Furthermore, the onset of a major weight loss occurs at higher temperatures for both samples and is more profound for the pH 2 and pH 3 synthesized samples, indicating moderate thermal stability,[85] compared to the pH 3 and pH 2 samples.

The DSC curves in Fig. 7(a), however, revealed the thermal transitions and phase changes occurring in the nanocomposite under different pH conditions. The endothermic and exothermic peaks correspond to events such as the reduction of iron oxides, phase transformations of TiO_2, and interactions between the nZVI, SiO_2, and TiO_2 components.[70] The positions

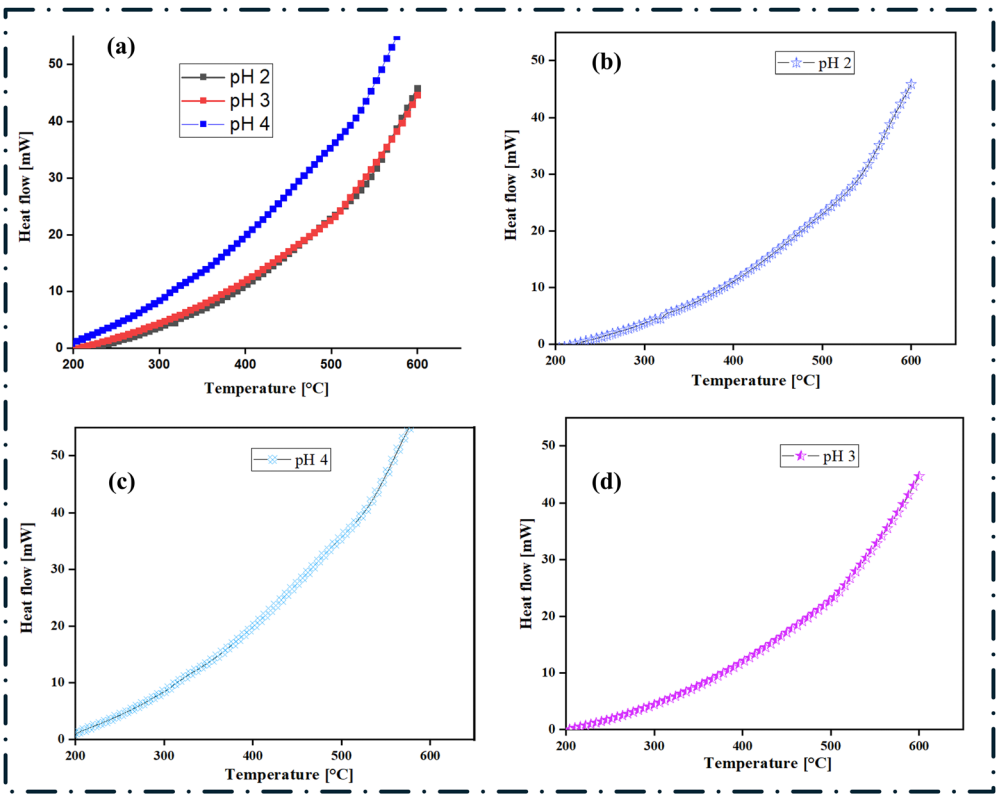

Fig. 7 Differential scanning calorimetry (DSC) analysis of SiO_2–TiO_2–nZVI nanocomposites synthesized under different pH conditions. (a) Stacked comparison of the thermal behaviour of SiO_2–TiO_2–nZVI under all three reaction conditions; (b) thermal behaviour of SiO_2–TiO_2–nZVI at pH 2; (c) thermal behaviour of SiO_2–TiO_2–nZVI at pH 3 and (d) thermal behaviour of SiO_2–TiO_2–nZVI at pH 4.

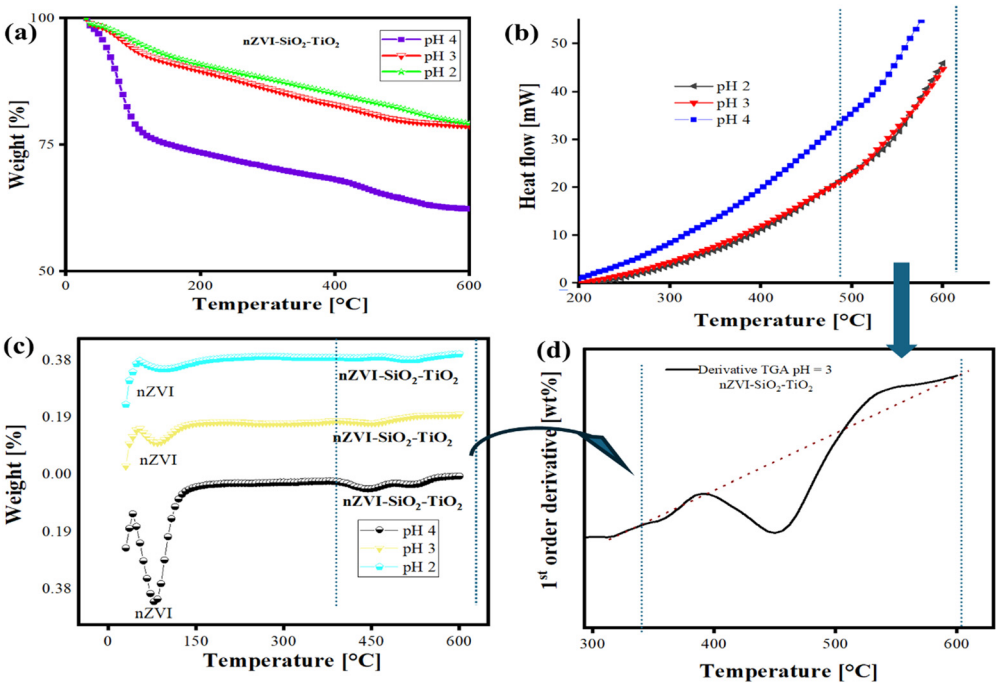

Fig. 8 Thermogravimetric analysis (TGA) and comparison of the thermal properties and characteristics of nZVI–SiO_2–TiO_2 nanocomposites. (a) Stacked TGA plots, (b) stacked DSC plots and (c) and (d) TGA weight percent derivatives.

and intensities of these thermal events vary significantly between the pH conditions, suggesting that the pH of the environment influences the phase composition and interactions within the nanocomposite.[86,87] The weight loss curves reported for the individual nZVI and the novel nZVI–SiO_2–TiO_2 components show distinct differences, and the nZVI component exhibits a sharp weight loss at around 400 °C, corresponding to the oxidation of zero-valent iron. In the nZVI–SiO_2–TiO_2 nanocomposite, this oxidation event is shifted to higher temperatures and occurs in a more gradual manner, indicating improved thermal stability and oxidation resistance of the nZVI phase.[88] The derivative TGA plot in Fig. 8(d) shows the rate of weight loss as a function of temperature for the nZVI–SiO_2–TiO_2 nanocomposite at pH 3. This plot provides additional insights into the thermal decomposition stages and the influence of the different components on the overall thermal behaviour. The multiple peaks and inflection points in the derivative TGA curve suggest the occurrence of complex thermal events and molecular interactions[89] within the nZVI–SiO_2–TiO_2 nanocomposite.

3.4 Catalytic activity and performance evaluation using methylene blue dye degradation experiments

MB dye solutions with varying concentrations of 3 ppm, 5 ppm, and 10 ppm were prepared following the procedure described in Section 2.3. MB dye concentrations were subsequently reassessed using UV-vis spectroscopy at 10-minute intervals.

The removal efficiencies (%) and quantity of MB dye removed were computed using the following mass balance relations:

$$q_e = \frac{(C_0 - C_e) \times V}{m} \quad (2)$$

$$\text{Removal efficiency } (\%) = \frac{C_0 - C_e}{C_0} \times 100 \quad (3)$$

where C_0, C_e are the initial and equalization dye concentrations (mg L^{-1}), V is the bulk volume (L) of MB dye solution and m is the mass (g) of nZVI–SiO_2–TiO_2.

The results in Fig. 9 and 10 show the performance of the nZVI–SiO_2–TiO_2 nanocomposite in MB dye removal at different time intervals and MB dye concentrations and the amount of MB dye adsorbed at a given time, t (min). The nZVI–SiO_2–TiO_2 nanocomposite synthesized under pH 2 reaction conditions (Fig. 9(c)) exhibited the fastest dye degradation rate with the maximum removal efficiency reaching up to 100% in 20 min for 3 ppm MB dye solution and 99.6% and 98.9% for 5 and 10 ppm after 20 min, respectively.

The steep slope curves of the nanocomposite synthesized at pH 2 indicate rapid degradation of the methylene blue dye, removing >90% of the dye in the first 10 minutes. This suggests the excellent catalytic activity of the nZVI–SiO_2–TiO_2 nanocomposites and their promising applications for environmental remediation.[73] The catalytic performance of the nanocomposite synthesized under the pH 2 condition is consistent with the findings from the materials characterizations described in Section 2.3, including IR, FESEM, EDS, BET, XRD, TGA, and DSC. The pH 2 synthesized nanocomposite displayed moderate thermal stability, structural integrity, and significant synergistic interactions of the nZVI, SiO_2, and TiO_2 components in the nanocomposite. These exceptional characteristics accounted for its enhanced catalytic activity[90] and dye removal efficiency.[91] The nanocomposite samples synthesized

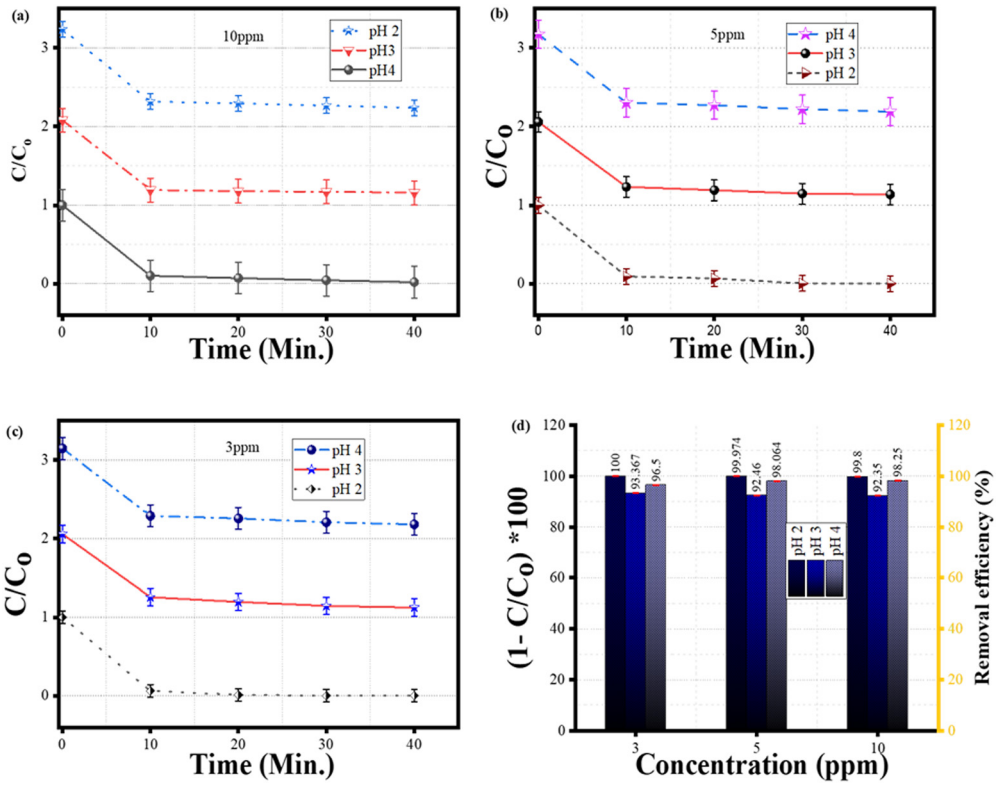

Fig. 9 Performance of the nZVI–SiO_2–TiO_2 nanocomposite in the degradation and removal of methylene blue dye at different methylene blue dye concentrations: (a) 10 ppm methylene blue dye concentration, (b) 5 ppm methylene blue dye concentration and (c) 3 ppm methylene blue dye concentration. (d) Dye removal efficiencies *versus* concentrations.

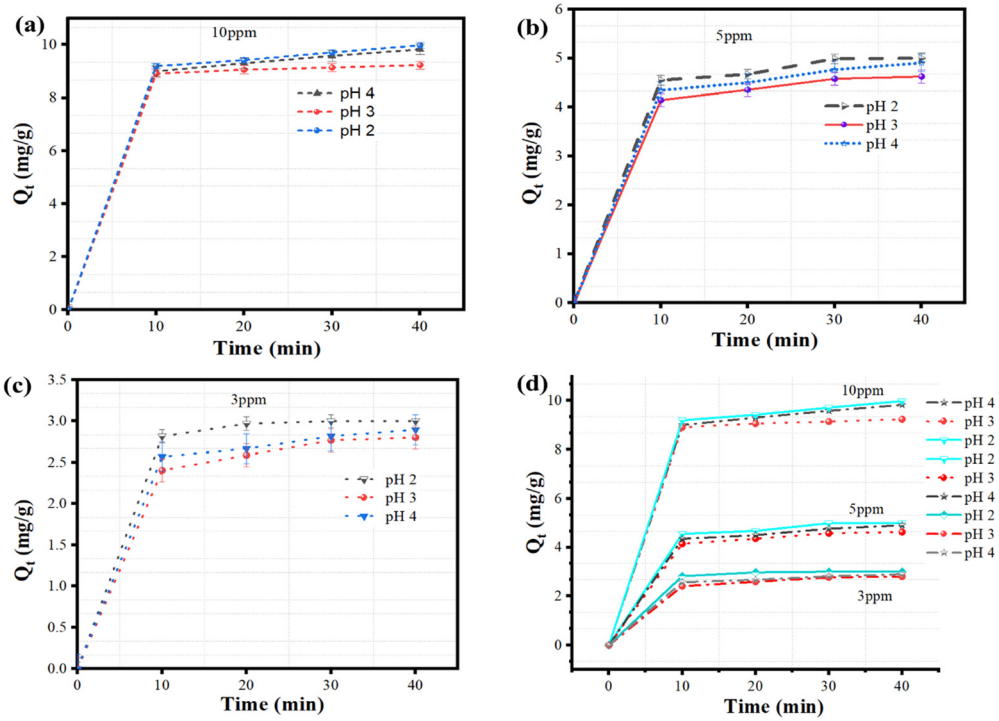

Fig. 10 Amount (mg g^{-1}) of MB dye adsorbed per unit mass of nZVI–SiO_2–TiO_2 at a given time, *t* (min). (a)–(c) The amount of MB dye adsorbed at a given time for C_0 = 10 ppm, C_0 = 5 ppm and C_0 = 3 ppm; (d) comparison of the quantity adsorbed at different dye concentrations.

under pH = 3 and pH = 4 conditions show low dye degradation efficiencies of 96% and 97% compared to the pH = 2 sample. This is evident from the less steep slopes of the corresponding curves in Fig. 10(a) and (b) during the first 10 minutes of the dye degradation reactions. Furthermore, the dye removal efficiency decreases as the synthesis pH was increased from 2 to 4, with the pH = 4 nanocomposite sample exhibiting the lowest overall removal performance. The plot of the amount of MB dye (mg g^{-1}) adsorbed *versus* contact time presented in Fig. 10(a)–(d) further compared and confirmed the superiority in the performance of the pH 2 synthesized nanocomposite.

3.5 TGA activation energy analysis

To determine the reusability of the spent catalysts and the range of their thermal stability, TGA activation energy analysis was conducted (see Fig. 11). This was done by simplifying and applying the Arrhenius equation to all nZVI–SiO_2–TiO_2 nanocomposites synthesized under pH 4, pH 3 and pH 2, respectively.

The Arrhenius plots for the nZVI–SiO_2–TiO_2 nanocomposite samples show a linear relationship between the logarithm of the rate constant ($\ln(k)$) and the inverse of temperature ($1/T$), while the slopes of the linear fits in Fig. 11(b)–(d) provide the activation energy (E_a) for the thermal degradation process of the materials. The TGA activation energies of 54 kJ mol^{-1}, 58 kJ mol^{-1}, and 61 kJ mol^{-1} when decreasing from pH 4 to pH 2 suggest the facilitation of thermal degradation reactions within the nZVI–SiO_2–TiO_2 nanocomposites at lower pH, which can be associated to the synergistic properties of nZVI, SiO_2, and TiO_2 components, as well as the possible enhanced redox reactions and catalytic activity under these conditions, thus potentially making nZVI–SiO_2–TiO_2 nanocomposites reusable and suitable for thermally demanding processes.

3.6 Reusability experiment

The reusability of SiO_2–TiO_2–nZVI nanocomposites for MB dye removal was investigated following the procedure described in ref. 92 with little modification. Briefly, after the first cycle (as described in Section 2.3), the SiO_2–TiO_2–nZVI nanoparticles were centrifuged at 4000 rpm and 25 °C temperature. The dye laden SiO_2–TiO_2–nZVI particles were then washed with 90% ethanol solution several times and centrifuged again at 4000 rpm and room temperature before subsequent drying in a mini tube furnace under nitrogen conditions. The dried powder was reused as done in the previous performance test and the procedure was repeated following each cycle. In this recyclability test, 5 cycles

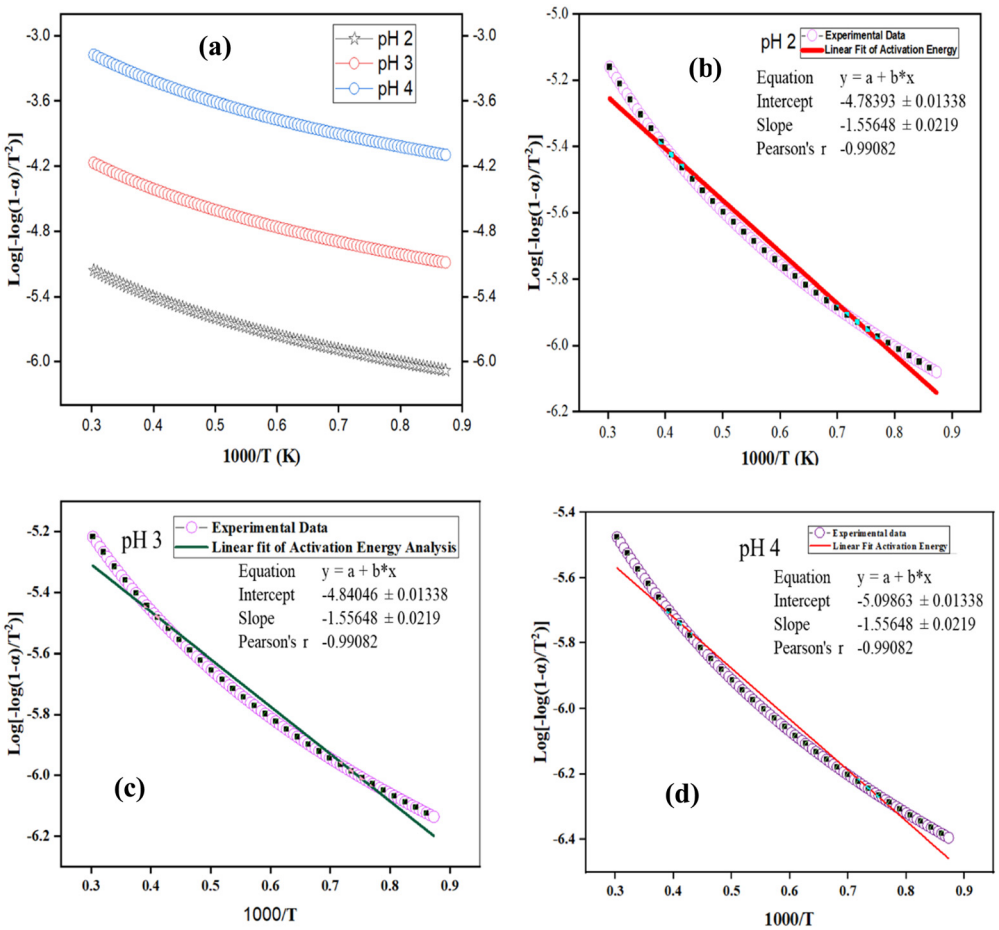

Fig. 11 TGA activation energy analysis of nZVI–SiO_2–TiO_2 (a), linear fit at pH 2, (b) linear fit at pH 3 and (c) linear fit at pH 4 (d).

were considered in evaluating the sorption capacities with respect to the number of cycles as shown in Fig. 12.

The sorption capacities of SiO_2–TiO_2–nZVI nanocomposites after 5 successive sorption–desorption cycles declined from 9.42 to 8.93 mg g^{-1} (4.9%) for the sample synthesized at pH 2, 9.07 to 7.71 mg g^{-1} (13.6%) for the sample synthesized at pH 3, and 9.28 to 7.897 mg g^{-1} (13.8%) for the sample synthesized at pH 4. The observed trend is associated to the strength of chemical bonds between SiO_2, TiO_2, and nZVI. Another factor is oxidation coupled with a significant amount of hydroxyl group generation during the desorption process.[92,93] Fig. 13 reveals the influence of synthesis pH on the equilibrium adsorption for SiO_2–TiO_2–nZVI nanocomposites synthesized at different pH values.

These findings (from Fig. 12 and 13) further unveiled the considerable influence of synthesis pH on both the performance and regenerative properties of the synthesized nanocomposites. However, the sorption capacities of SiO_2–TiO_2–nZVI nanocomposites were found to decrease slightly during the sorption–desorption process, and among them, the sorption capacity of the SiO_2–TiO_2–nZVI nanocomposite synthesized at pH 2 declined about 3 times compared to the subsequent pH values (see Fig. 13), indicating high performance and stability of iron materials synthesized under this reaction condition.[94] In conclusion, the recyclability and recoverability test corroborated the economic potential of the SiO_2–TiO_2–nZVI nanocomposite for wastewater remediation unveiling the distinctive abilities of the material to be used and reused with high sorption capacities. These distinctive sorption and physicochemical properties of SiO_2–TiO_2–nZVI were further compared with other emerging

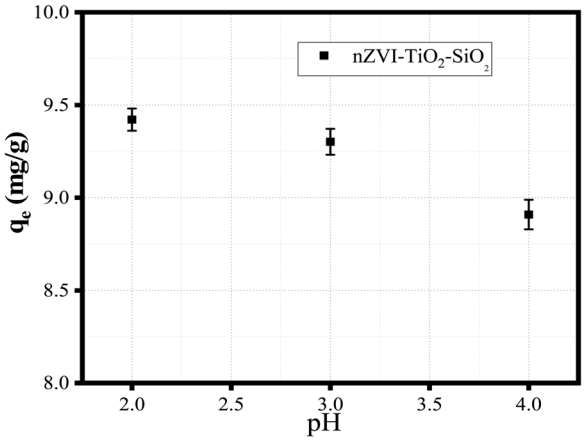

Fig. 13 Influence of synthesis pH on the equilibrium adsorption, q_e (mg g^{-1}), of SiO_2–TiO_2–nZVI nanocomposites.

sorbent materials such as the $MgFe_2O_4$/polyaniline nanocomposite developed to remove methyl red dye[95] and modified jarul bio-char/polypyrrole (CLSHB/PPy) for the treatment of pharmaceutical effluent,[96] among others reported in the literature. Table 3 compares the efficiencies and other imperative adsorption parameters of the developed SiO_2–TiO_2–nZVI nanocomposites with other adsorbents for removal of MB dye.

3.7 Sorption mechanism

Fig. 14 shows the FTIR spectra of the SiO_2–TiO_2–nZVI nanocomposites before and after sorption. From this figure, the

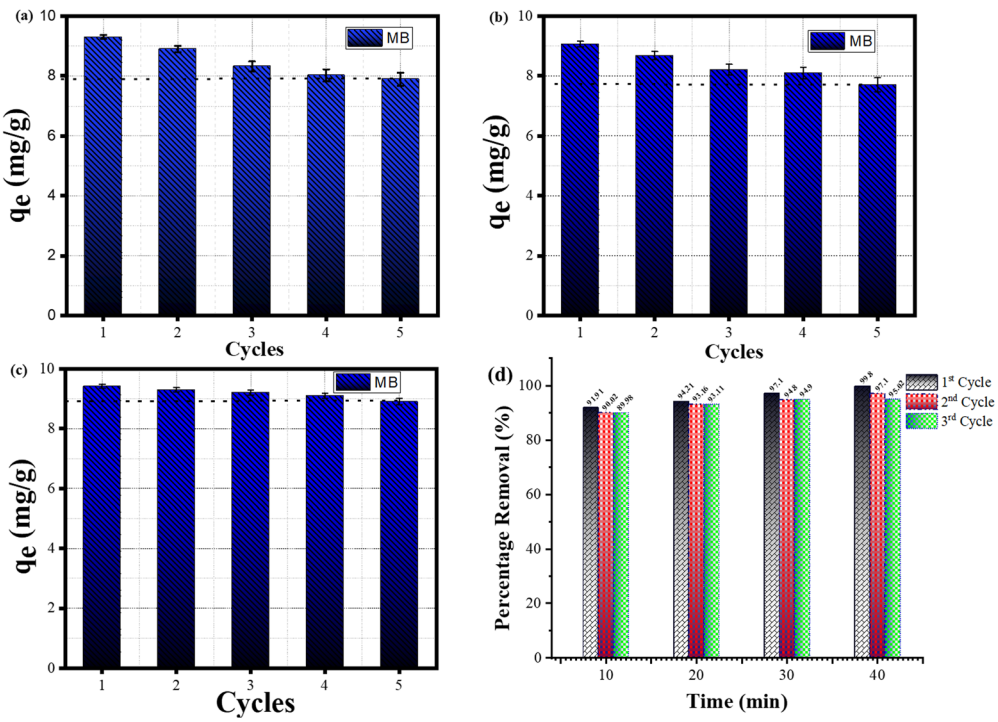

Fig. 12 Sorption capacities of MB dye by SiO_2–TiO_2–nZVI nanocomposites after five successive cycles: (a) SiO_2–TiO_2–nZVI at pH 4, (b) SiO_2–TiO_2–nZVI at pH 3, (c) SiO_2–TiO_2–nZVI at pH 2 and (d) percentage MB removal per time in the first three regenerative cycles.

Table 3 Comparison of SiO_2–TiO_2–nZVI and other adsorbent materials reported in the literature for MB dye removal

Catalyst materials	Light sources	Catalyst conc. (mg L^{-1})	Dye conc. (mg L^{-1})	Efficiency (%)	Contact time (minutes)	Ref.
SiO_2–TiO_2–nZVI	No light source used	0.1	3, 5 and 10	99.8	20	This study
Fe_3O_4@SiO_2–TiO_2	UV 365 nm, 6 × 8 W	1	1	93	90	97
MNP@SiO_2@TiO_2	UV 365 nm, 80 W, Hg	0.56	3.2	94.8	30	98
γ-Fe_2O_3/SiO_2/C-TiO_2	Sunlight	3.5	5	96.8	180	99
γ-Fe_2O_3/SiO_2/GSs/TiO_2	UV	3.5	5	77.1	180	100
γ-Fe_2O_3/SiO_2/GSs/TiO_2	UV	0.04	20	66	30	100

characteristic peaks observed from 1000 to 1060 cm^{-1} in Fig. 11a, corresponding to the Si–O–Ti asymmetric or Si–O–Si symmetric stretching vibrations, are seen to be stretched, broadened and negatively shifted to around 980 cm^{-1} in Fig. 14(b) after sorption with the increase of pH from 4 to 2. This indicates surface interactions of the hydroxyl (Ti–O–H) and silanol groups (Si–O–H) with the amino and/or sulphur functional groups present in MB dye molecules.[101] The adsorption of MB dye on these metal oxide surfaces could result in a bathochromic (red) shift of the MB absorption spectrum due to changes in the electronic transitions of the MB dye upon adsorption on the nZVI–SiO_2–TiO_2 surface,[98] corroborating the bond transformation as the MB dye is being adsorbed on the surface of SiO_2–TiO_2–nZVI nanocomposites. The aromatic rings of the MB dye sustained by sulphur and nitrogen heteroatoms are likely broken during this bond transition, resulting in the breakage of S–Cl bonds and initiating the dye degradation process and formation of MB^+ molecules.[102] It is imperative to note that no significant bathochromic shift of the peaks was observed for the SiO_2–TiO_2–nZVI nanocomposite synthesized at pH 4 after the sorption procedure, and this confirmed the influence of synthesis pH on the possible reaction potential of the SiO_2–TiO_2–nZVI nanocomposite. The peaks at 400 to 500 cm^{-1} were completely shifted after the adsorption procedure as shown in Fig. 14(b). These peak shifts are associated with increased dye adsorption on the nanocomposite surface due to large hydroxyl group interactions with MB dye molecules at the heterogeneous surface of SiO_2–TiO_2–nZVI and possible interactions between Fe^0 and the sulphur functional group of MB dye molecules, resulting in subsequent reduction of Fe^0 to Fe^{2+} or disappearance of undissociated dye (MB^0) species. This reduction and presence of hydroxyl groups enhances complete oxidation of MB dye–methyl components and the subsequent hydroxylation of the sulphonated components of the dye molecules.[103] The peak at 2360 cm^{-1} is associated with Ti–O–Fe bonds from TiO_2, and nZVI shrinks after sorption as shown in Fig. 14b. This could indicate possible formation of reactive oxygen species (ROS) from nZVI due to electron support from the surface of TiO_2, resulting in ROS interactions with the cationic MB site.[104] Peaks observed at 2900 cm^{-1} for nanocomposites before sorption (Fig. 14(a)) are completely stretched after adsorption (Fig. 14(b)), while the peak at 3737 cm^{-1} was shifted after adsorption which could be associated with the π–π interactions between the aromatic rings of MB dye[105] and the heterogeneous surface of the SiO_2–TiO_2–nZVI nanocomposites. In conclusion, methylthioninium chloride or simply MB dye interacted with the SiO_2–TiO_2–nZVI nanocomposite surface through adsorption and reduction reactions.

The possible chemical reactions are divided into adsorption, chemical reduction and possible photocatalytic reactions due to the presence of TiO_2 which is not investigated in this study. The porous and high surface area of SiO_2 and TiO_2 provided abundant adsorption sites for the MB dye molecules. While methylene blue molecular adsorption occurs through hydrogen bonding, electrostatic interactions, and coordination bonding between the functional groups on the heterogeneous SiO_2–TiO_2–nZVI adsorbent surfaces and the MB dye, the Fe^0 in the nZVI directly reduces the adsorbed MB dye molecules through heterogeneous electron transfer. The reduced iron species (Fe^{2+}) further reacts with hydrogen peroxide (H_2O_2) to generate additional hydroxyl radicals ($OH^•$) through the Fenton-like reaction.

Possible reaction mechanisms are as follows:

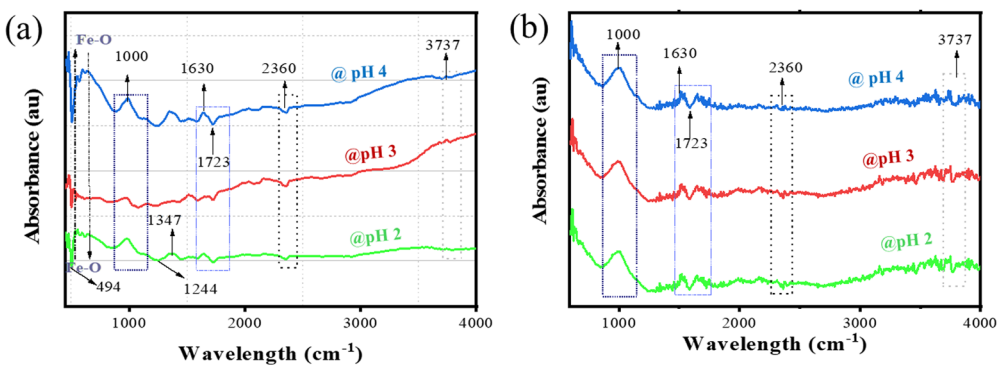

Fig. 14 FTIR spectra of the nZVI–SiO_2–TiO_2 nanocomposites before (a) and after (b) MB dye degradation.

$$Si–OH + C_{16}H_{18}ClN_3S \rightarrow Si–O–C_{16}H_{18}ClN_3S + H^+ \quad (4)$$

$$Ti–OH + C_{16}H_{18}ClN_3S \rightarrow Ti–O–C_{16}H_{18}ClN_3S + H^+ \quad (5)$$

$$Ti–O–C_{16}H_{18}ClN_3S^+ \rightarrow Ti–O–C_{16}H_{18}ClN_3S \quad (6)$$

Redox reactions with nZVI are as follows:

$$Fe^0 + C_{16}H_{18}ClN_3S^+ \rightarrow Fe^{2+} + \text{reduced } C_{16}H_{18}ClN_3S \quad (7)$$

$$Fe^0 + H_2O \rightarrow Fe^{2+} + 2HO^- \quad (8)$$

$$Fe^{2+} + H_2O_2 \rightarrow Fe^{3+} + OH^\bullet + OH^- \quad (9)$$

$$OH^\bullet + C_{16}H_{18}ClN_3S \rightarrow \text{degradation products} \quad (10)$$

3.7.1 Predominant sorption mechanism and thermodynamic parameters. To evaluate the influence of temperature on the physicochemical properties and the sorption of MB dye on the nZVI–SiO_2–TiO_2 nanocomposite, the thermodynamic parameters of the nanocomposite were investigated. The thermodynamic parameter studies were conducted using 0.01 mg L^{-1} of the synthesized nZVI–SiO_2–TiO_2 material at four different temperatures of 303 K, 313 K, 323 K, and 333 K with a fixed contact time of 40 minutes between the adsorbent and the MB dye solution. The van't Hoff equation was employed.

$$\ln(K_d) = -\frac{\Delta H}{RT} + \frac{\Delta S}{R} \quad (11)$$

$$\Delta G = \Delta H - T\Delta S \quad (12)$$

$$K_d = \frac{q_e}{C_e} \quad (13)$$

where K_d is the adsorption equilibrium constant; ΔG is the Gibbs free energy; ΔH is the corresponding change in enthalpy; ΔS is the change in entropy of the material; R (= 8.341) is the gas constant (kJ mol^{-1} K^{-1}); and T is the dye solution temperature in Kelvin.

Thermodynamic parameters, *viz.* the Gibbs free energy of adsorption (ΔG°), enthalpy change (ΔH°), and the entropy change (ΔS°), were evaluated from the slope and intercept of Fig. 15. Fig. 12 shows the relationship between the sorption equilibrium constant, $\ln(K_d)$, and the inverse temperature ($1/T$). The enthalpy value gives insight into the predominant adsorption mechanism. ΔH° values for physical adsorption are basically below 4.2 kJ mol^{-1}, whereas for predominant chemical adsorption, ΔH° values exceed 21 kJ mol^{-1}.[106] Hence, ΔS and ΔH (46.15 kJ mol^{-1}) obtained from the slope and intercept of Fig. 12 confirmed the dominant chemisorption nature of MB dye sorption on the nZVI–TiO_2–SiO_2 surface. Subsequently, the Gibbs free energy, ΔG, at various temperatures was evaluated (see Table 4). The negative sign in ΔG which declined with increasing temperature indicates the spontaneity of the MB dye sorption process on the nZVI–SiO_2–TiO_2 nanocomposite surface. This spontaneity and the negative sign in ΔG trends are characteristic properties of ZVI nanocomposite materials reported for a plethora of environmental remediation applications.

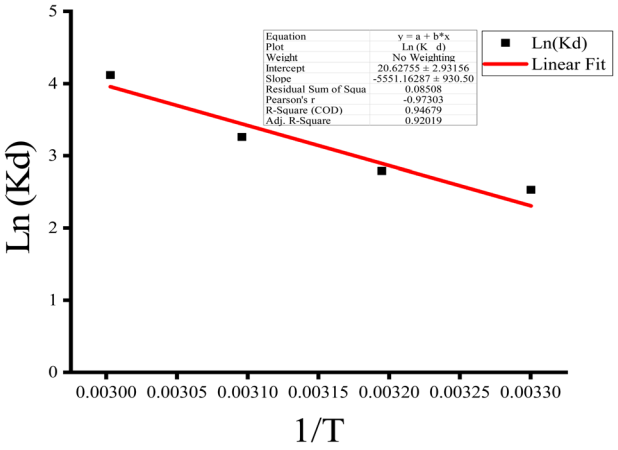

Fig. 15 Sorption thermodynamic parameters of MB dye sorption on the nZVI–TiO_2–SiO_2 nanocomposite.

3.7.2 Synergistic effects. The adsorption of MB on the SiO_2–TiO_2–nZVI nanocomposite surface was observed to attract the MB dye molecules into proximity with the redox-active nZVI sites, enhancing the occurrence of the reduction reactions. The SiO_2 component of the nanocomposite provides sufficient hydroxyl groups and a high surface area,[38] resulting in an enhanced adsorption capacity for MB dye on the nanoadsorbent of up to 100% (refer to Fig. 9 and 10). This occurred due to improved electrostatic interactions and hydrogen bonding between MB dye molecules and the nZVI–SiO_2–TiO_2 nanocomposite surface. The possible photocatalytic activity in the adsorption sites of TiO_2 components can be improved by the electron-trapping ability of nZVI,[97,98] which could lead to the generation of more reactive oxygen species.[107] Subsequently, the magnetic properties of nZVI[108] enabled easier separation and recovery of the nZVI–SiO_2–TiO_2 nanocomposites. These synergistic properties distinguished our novel material and enabled efficient and improved reutilization of the SiO_2–TiO_2–nZVI adsorbent. Table 5 compares these synergistic effects with other reported nanoadsorbent materials.

3.7.3 Analysis of the MB dye aggregation state and speciation behaviour under varying pH conditions. The potential changes and aggregation state of MB dye molecules during the degradation process in the presence of the novel SiO_2–TiO_2–nZVI nanocomposites were investigated before and after treatment. Fig. 16 shows the adsorption spectrum of MB dye solutions adsorbed following UV-vis analysis. The degradation

Table 4 Thermodynamic properties of MB dye sorption onto the nZVI–SiO_2–TiO_2 nanocomposite at 303–333 K

Temperature (K)	ΔG (kJ mol^{-1})	ΔH° (kJ mol^{-1})	ΔS° (kJ mol^{-1})
303	−5.811359461	46.15237	0.171497
313	−7.526333968		
323	−9.241308475		
333	−10.95628298		

Table 5 Comparison of the synergistic effects of nZVI–SiO_2–TiO_2 with other adsorbents

	Previous studies	nZVI–TiO_2–SiO_2 (this study)	Ref.
Adsorbent performance and contact time	He *et al.* used *Klebsiella oxytoca* biosorbent for MB dye removal. The adsorption capacities of both LRC and DRC toward MB dye reached about 90%. nZVI-biochar was studied by Zeng *et al.* (2023); the reduction reaction equilibrium was achieved after 100 min Xu *et al.* used nZVI-PCB for the adsorption and reduction of chromium. They reported a contact time of 220 minutes prior to equilibrium reaction concentration.	The nZVI component of SiO_2–TiO_2–nZVI facilitated reduction–oxidation reactions, completely (100%) degrading and mineralizing the dye compounds within a short period (20 min).	109–111
Magnetic separation	Rajabathar *et al.* recorded 97% MB dye removal efficiency under sunlight using Fe–TiO_2 within 40 min. The authors reported no significant magnetic properties during reusability analysis.	The presence of nZVI provided magnetic properties to the nZVI–TiO_2–SiO_2 nanocomposite, thereby enhancing separation and recovery of the adsorbent material and amplifying the overall water treatment process.	103
Reusability and cost effectiveness	Bahrami *et al.* utilized a microplastic adsorbent for the removal of MB dye from contaminated wastewater; the microplastic adsorbent catalyst material exhibited 74% dye removal after 5 regenerative cycles.	The developed SiO_2–TiO_2–nZVI adsorbent has shown significant prospects when regenerated and reused for multiple cycles (93% to 85% in five cycles) improving the overall cost-effectiveness and sustainability of the dye contaminated wastewater operations.	106
Synergistic effects with an enhanced adsorption capacity	Inamdar *et al.* reported 92% Congo red dye removal using tetragonal titania nanoparticles (TiO_2 NPs)	Silica (SiO_2), titanium dioxide (TiO_2), and nanoscale zero-valent iron (nZVI) provide a high surface area and diverse adsorption sites resulting in an improved dye adsorption capacity greater than 99% compared to individual components.	102

experiment followed the procedure described in ref. 112 with little modification. The modified procedure briefly involves the preparation of standard solution (10 ppm) separately. Subsequently, 0.003 g of the nanocomposites (synthesized at pH 2, 3, and 4) were introduced into 3 separate beakers (250 mL capacity), each containing 30 mL of 10 ppm dye solution at a fixed pH (6.0). The resulting mixture was stirred for 40 minutes and centrifuged at 4000 rpm for 5 min under room temperature to separate the dye laden particles from the treated dye solutions. The procedure was repeated and the absorbance was immediately measured after every cycle.

In Fig. 16(a), the presence of a shoulder near the monomer peaks indicating the presence of MB aggregated molecules is associated to the presence of trimers and/or higher MB dye aggregates. Similar patterns were observed by Kobayashi *et al.* (1989). In Fig. 12b, after dye degradation, the monomeric peaks were shifted from 664 nm in Fig. 16(a) towards shorter wavelengths to the dimer peaks at 605 nm (see Fig. 16b). This is due to the heterogeneous surface nature and the precipitation properties of the SiO_2–TiO_2–nZVI nanocomposites, generating small sizes of MB dye aggregates after encountering the nanocomposite surface functional groups.[112] No higher MB dye aggregates, trimers and/or tetramers were observed after treatment with SiO_2–TiO_2–nZVI. Potentially, degradation of MB dye by SiO_2–TiO_2–nZVI occurred through monomer mineralization and formation of a small amount of MB dimer precipitates. However, the pH of MB dye solution can potentially impact the electronic charge distributions on the heterogeneous surface of SiO_2–TiO_2–nZVI materials, hence influencing both the electrostatic interactions between MB dye molecules and the nanocomposites, as well as speciation of MB dye molecules in the solution. Therefore, the MB dye speciation analysis was conducted. The speciation of MB dye molecules (see Fig. 17) describes the relative abundance of two major MB dye species,

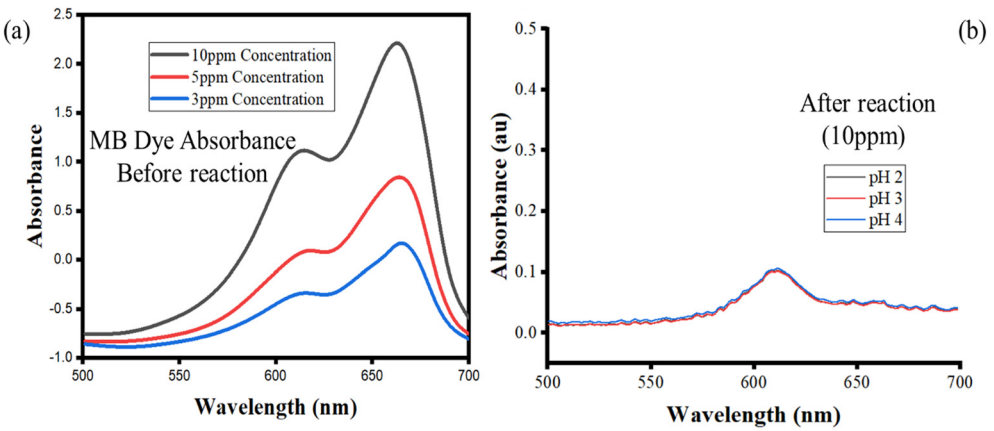

Fig. 16 MB dye adsorption spectra before (a) and after (b) exposure to SiO_2–TiO_2–nZVI nanocomposites.

viz. the cationic form or MB^+ and the undissociated molecule or MB^0, as a function of solution pH. At a lower pH of MB solution (2 and 3), from Fig. 17(a)–(c), undissociated MB species (MB^0) predominated (>80%) for both nanocomposite samples. At pH 4, both MB^0 and MB^+ coexisted with the SiO_2–TiO_2–nZVI nanocomposite synthesized at pH 2 having a slightly greater proportion of MB^+ species at a lower pH (Fig. 17(d)). At pH = pK_a, mineralized and undissociated MB dye species coexist in equilibrium. Above pH = 5.8, all the MB dye species were dissociated, and no undissociated MB^0 is present in both nanocomposite samples. In conclusion, solution pH was observed to significantly influence the mineralization and/or formation of undissociated MB dye molecules and these findings are in conformity with the results of Sun *et al.*[105] Lower solution pH values favoured the formation of undissociated MB species and *vice versa*.[113] The nanocomposite synthesis pH progressively influenced the overall interactions of the SiO_2–TiO_2–nZVI nanocomposite material with MB dye molecules favouring the formation of MB^+ species.

3.8 Economic analysis

Prior to industrial or large-scale application of SiO_2–TiO_2–nZVI, apart from the promising performance of this novel material, it is imperative to consider the cost and feasibility of SiO_2–TiO_2–nZVI for industrial/large-scale purposes. The production of SiO_2–TiO_2–nZVI requires the utilization of primary chemicals mentioned in the list of materials above, namely, silica, titania, iron precursor, reducing agents and other additional solvents. The cost and availability of these chemicals are highly imperative and play a significant role in performing a cost analysis for industrially producing this novel material. The major constituent (adsorbent) of SiO_2–TiO_2–nZVI is zero valent iron or nZVI. There are existing companies engaged in large-scale production of nZVI,[114] each providing different options in terms of particle size, specific surface area, forms, and cost. Apart from the procurement cost of nZVI, SiO_2, and TiO_2, one must also consider expenses related to additional laboratory and field experiments, hydrogeological and geochemical studies, as well as pilot testing in contaminated areas.[115] Therefore, analysing the total cost (see Table 6) involved in implementing a technology that utilizes SiO_2–TiO_2–nZVI is a complicated process that relies on various factors, including the type of product, order quantity, and transportation costs. A pilot study could serve as an initial step in gathering practical information needed for carrying out a successful scale-up of a remediation process. In the case of nZVI, the initial pilot trial use of nZVI was conducted in Trenton, USA, where 2.5 kg of modified Pd/nZVI was used at a concentration of 1 g L^{-1} to purify groundwater contaminated with chloroform among other contaminants. After 4 weeks of treatment, a 96.5% reduction in chloroorganic contaminants was achieved.[114]

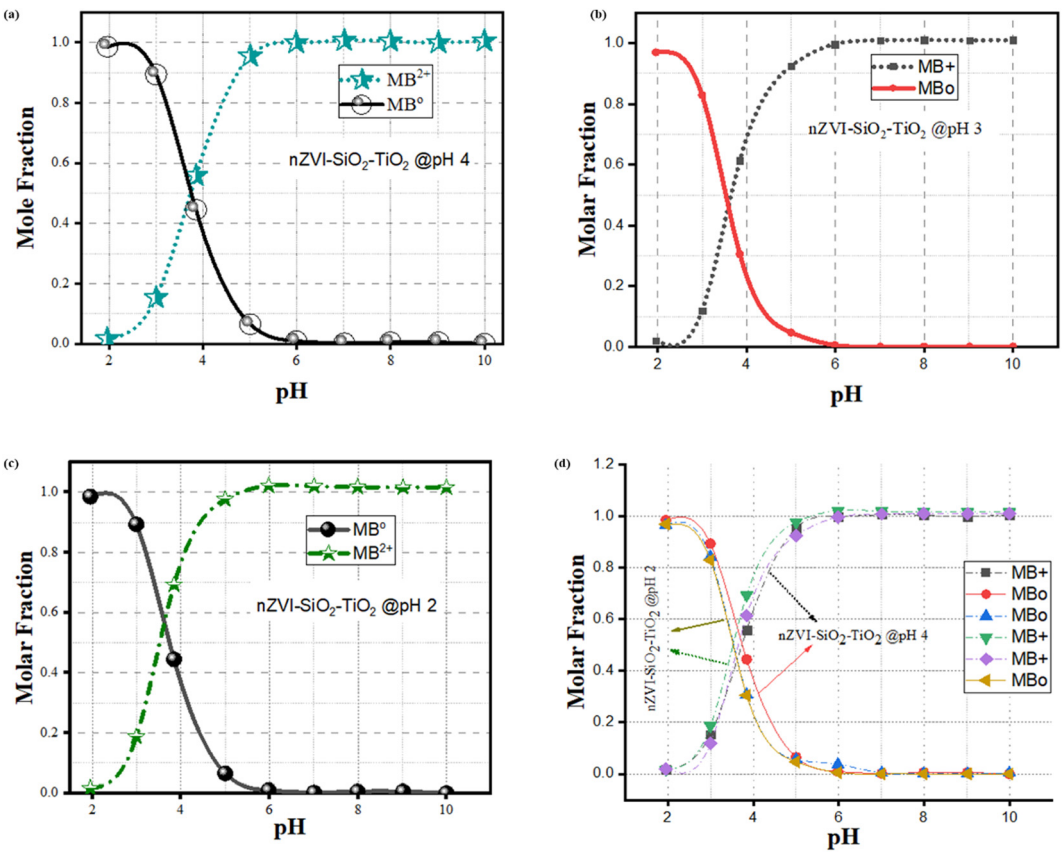

Fig. 17 Speciation behaviour of methylene blue dye following SiO_2–TiO_2–nZVI interaction under varying pH conditions: (a) pH 2, (b) pH 3, (c) pH 4, and (d) combined variable pH conditions, with an initial concentration of C_0 = 10 g L^{-1}.

Table 6 Cost evaluation for stages and chemicals used in the synthesis of the nZVI–TiO_2–SiO_2 nanocomposite

Stages of fabrication		Cost assignment	Materials and energy ($)	Cost per fabrication stage
Procurement of precursors	Procurement of iron precursor, SiO_2 precursor and titania oxide nanoparticles from transport, packaging and storage to usage	$Cost_{Proc}$	$80.5 per kg Fe(III) sulfate $0.4 per kg silica ($SiO_2$) $1.8 per gram TiO_2 nanoparticles ((80.5/1000) × 8.8) + (0.00208 + 9.36)	$9.36
Pretreatment of precursors	No further treatment required.	$Cost_{Pre}$	$0.0	$0.00
Chemical activation	Sodium hydroxide and hydrochloric acid solution control	$Cost_{Chem}$	$0.012	$0.012
Chemical reduction of iron precursor and formation of nZVI–TiO_2–SiO_2	Reducing agent ($NaBH_4$). Nitrogen (N_2) flow	$Cost_{Cred}$	$1.41 per gram $NaBH_4$ (1.41 × 1.89) = $2.66	$2.66
Centrifugation and tube furnace drying	Washing, heating, nitrogen (N_2) flow	$Cost_{Drying}$	Energy cost + nitrogen flow $0.21	$0.21
Other costs	Offset cost Miscellaneous cost	$Cost_{other}$	10% of $(9.36 + 0.012 + 2.66 + 0.21)	$1.22
Total				$13.46

The successful outcomes from pilot trials increased efforts in utilizing nZVI and its composite materials for full-scale water and soil remediation.

For brevity, although there are no existing SiO_2–TiO_2–nZVI nanocomposite plants, following the method described in ref. 116, the economic analysis (see Table 6) indicates that the SiO_2–TiO_2–nZVI composite adsorbent might be expensive compared to certain conventional adsorbents like clay minerals. Nonetheless, its exceptional ability to adsorb and be recycled could counterbalance the higher upfront expenses, potentially making it a feasible choice for water and wastewater treatment purposes. Scale-up studies, *via* methods such as batch adsorption studies,[117] for the nZVI–SiO_2–TiO_2 nanocomposite material are recommended for future research to better capture the actual cost requirement for large-scale industrial applications.

4 Conclusion

In conclusion, the novel SiO_2–TiO_2–nZVI nanocomposite was synthesized using three different synthesis pH values (2, 3, and 4) *via* a combined chemical reduction method. The synergistic effects of nZVI, SiO_2, and TiO_2 on the novel SiO_2–TiO_2–nZVI nanocomposites were unveiled through MB dye degradation experiments. Analysis and characterization techniques including FTIR, SEM, EDS BET, XRD, DSC and TGA corroborated the influence of synthesis pH on the structural integrity, crystallinity, and interfacial interactions of the nZVI, SiO_2, and TiO_2 components within the novel SiO_2–TiO_2–nZVI nanocomposite. These favourable physicochemical properties are more pronounced on the SiO_2–TiO_2–nZVI nanocomposite synthesized under pH 2 conditions. The enhanced catalytic activity due to the synergistic effect observed in the dye degradation experiments enabled up to 100% methylene blue dye removal with reusability performance greater that 90%. The sorption mechanism and MB dye speciation tests show the synergistic adsorption and reduction ability of SiO_2–TiO_2–nZVI and a significant influence of pH on the mineralisation and formation of undissociated MB species. The synthesized SiO_2–TiO_2–nZVI nanocomposites recorded 100% presence of MB^+ species in MB solution above pH 6.0. These findings highlight the crucial role of pH in governing the synthesis, thermal stability, interfacial interactions, and catalytic activity of the SiO_2–TiO_2–nZVI nanocomposite, accentuating the importance of optimizing the synthesis conditions of emerging sorbents for efficient environmental remediation applications.

Data availability

The data supporting this article have been included as part of the ESI.†

Conflicts of interest

There are no conflicts to declare.

Acknowledgements

This work was funded by Universiti Malaysia Sarawak under Vice Chancellor Higher Impact Research Scheme (Grant No. UNI/FO2/VC-HIRG/85508/P10-03) and Princess Nourah bint Abdulrahman University Researchers Supporting (Project No. PNURSP2024R80), Princess Nourah bint Abdulrahman University, Riyadh, Saudi Arabia. The authors also wish to acknowledge the support of the FRST department of Universiti Malaysia Sarawak for their assistance in FESEM and EDX

analyses, Dr Ibrahim Yakub for his permission to use tube furnace, and Mr Airul Azhar Bin Jitai and Aysha, Department of Chemical Engineering and Energy Sustainability, for their support throughout the experimental analysis.

References

1 S. S. Muthu, Textiles and Clothing Sustainability: Nanotextiles and Sustainability, *Textile Sci. Clothing Technology*, 2017, p. 110. Available from: **http://www.springer.com/series/13111**.

2 G. A. Kallawar and B. A. Bhanvase, A review on existing and emerging approaches for textile wastewater treatments: challenges and future perspectives, *Environ. Sci. Pollut. Res. Int.*, 2024, **31**(2), 1748–1789, DOI: **10.1007/s11356-023-31175-3**.

3 H. Kamani, M. Hosseinzehi, M. Ghayebzadeh, A. Azari, S. D. Ashrafi and H. Abdipour, Degradation of reactive red 198 dye from aqueous solutions by combined technology advanced sonofenton with zero valent iron: characteristics/effect of parameters/kinetic studies, *Heliyon*, 2024, **10**(1), e23667, DOI: **10.1016/j.heliyon.2023.e23667**.

4 M. Namakka, M. D. R. Rahman, K. A. M. B. Said, M. Abdul Mannan and A. M. Patwary, A review of nanoparticle synthesis methods, classifications, applications, and characterization, *Environ. Nanotechnol., Monit. Manage.*, 2023, **20**, 100900, DOI: **10.1016/j.enmm.2023.100900%0A**.

5 K. O. Badmus, N. Irakoze, O. R. Adeniyi and L. Petrik, Synergistic advance Fenton oxidation and hydrodynamic cavitation treatment of persistent organic dyes in textile wastewater, *J. Environ. Chem. Eng.*, 2020, **8**(2), 103521, DOI: **10.1016/j.jece.2019.103521**.

6 K. P. Kowalski and E. G. Søgaard, Implementation of zero-valent iron (ZVI) into drinking water supply – Role of the ZVI and biological processes, *Chemosphere*, 2014, **117**(1), 108–114, DOI: **10.1016/j.chemosphere.2014.05.088**.

7 Y. F. Wang, B. Y. Gao, Q. Y. Yue, Y. Wang and Z. L. Yang, Removal of acid and direct dye by epichlorohydrin-dimethylamine: flocculation performance and floc aggregation properties, *Bioresour. Technol.*, 2012, **113**, 265–271, DOI: **10.1016/j.biortech.2011.11.106**.

8 S. Wang, J. Wang, A. Mishra and M. Bajpai, Electron beam radiation coupled to flocculation for advanced treatment of coking and dyeing wastewater: performance and synergistic effect, *J. Cleaner Prod.*, 2006, **454**, 142344, DOI: **10.1016/j.jclepro.2024.142344**.

9 F. R. Furlan, L. G. de Melo da Silva, A. F. Morgado, A. A. U. de Souza and S. M. A. Guelli Ulson de Souza, Removal of reactive dyes from aqueous solutions using combined coagulation/flocculation and adsorption on activated carbon, *Resour., Conserv. Recycl.*, 2010, **54**(5), 283–290.

10 M. Riera-Torres, C. Gutiérrez-Bouzán and M. Crespi, Combination of coagulation-flocculation and nanofiltration techniques for dye removal and water reuse in textile effluents, *Desalination*, 2010, **252**(1–3), 53–59.

11 A. James, M. Rezaur Rahman, K. Anwar Mohamed Said, M. Namakka, K. Kuok Kuok and M. Uddin Khandaker, *et al.*, Lithium Chloride-Mediated enhancement of dye removal capacity in Borneo bamboo derived nanocellulose-based nanocomposite membranes (NCMs), *J. Mol. Liq.*, 2024, **413**, 125973, DOI: **10.1016/j.molliq.2024.125973**.

12 R. Rahman, A. James and A. Mohamed, Polyvinylidene fluoride (PVDF) nanocomposite membrane for wastewater treatment by a photocatalytic process, *Mater. Adv.*, 2024, **5**(19), 7617–7636, DOI: **10.1039/d4ma00716f**.

13 R. Matthews, M. Winson and J. Scullion, Treating landfill leachate using passive aeration trickling filters; effects of leachate characteristics and temperature on rates and process dynamics, *Sci. Total Environ.*, 2009, **407**(8), 2557–2564, DOI: **10.1016/j.scitotenv.2009.01.034**.

14 D. Ziolko, D. Hala, J. N. Lester and M. D. Scrimshaw, The effectiveness of conventional trickling filter treatment plants at reducing concentrations of copper in wastewaters, *Sci. Total Environ.*, 2009, **407**(24), 6235–6241, DOI: **10.1016/j.scitotenv.2009.08.047**.

15 E. H. Khader, S. A. Muslim, N. M. C. Saady, N. S. Ali, I. K. Salih and T. J. Mohammed, *et al.*, Recent advances in photocatalytic advanced oxidation processes for organic compound degradation: a review, *Desalin. Water Treat.*, 2024, **318**, 100384, DOI: **10.1016/j.dwt.2024.100384**.

16 B. Yan, Y. Dai, L. Xin, M. Li, H. Zhang and H. Long, *et al.*, Research progress in the degradation of printing and dyeing wastewater using chitosan based composite photocatalytic materials, *Int. J. Biol. Macromol.*, 2024, **263**(P2), 130082, DOI: **10.1016/j.ijbiomac.2024.130082**.

17 T. Munawar, F. Mukhtar, K. M. Batoo, A. Mazhar, M. S. Nadeem and S. Hussain, *et al.*, Sunlight-activated Mo-doped La_2CuO_4/rGO perovskite oxide nanocomposite for photocatalytic treatment of diverse dyes pollutant, *Mater. Sci. Eng., B*, 2024, **304**, 117355, DOI: **10.1016/j.mseb.2024.117355**.

18 D. Fatta-Kassinos, M. I. Vasquez and K. Kümmerer, Transformation products of pharmaceuticals in surface waters and wastewater formed during photolysis and advanced oxidation processes – Degradation, elucidation of byproducts and assessment of their biological potency, *Chemosphere*, 2011, **85**(5), 693–709, DOI: **10.1016/j.chemosphere.2011.06.082**.

19 L. Rizzo, Bioassays as a tool for evaluating advanced oxidation processes in water and wastewater treatment, *Water Res.*, 2011, **45**(15), 4311–4340, DOI: **10.1016/j.watres.2011.05.035**.

20 C. R. Holkar, A. J. Jadhav, D. V. Pinjari, N. M. Mahamuni and A. B. Pandit, A critical review on textile wastewater treatments: possible approaches, *J. Environ. Manage.*, 2016, **182**, 351–366, DOI: **10.1016/j.jenvman.2016.07.090**.

21 A. Dąbrowski, Adsorption – From theory to practice, *Adv. Colloid Interface Sci.*, 2001, **93**(1–3), 135–224.

22 S. Das, S. Rudra Paul and A. Debnath, Fabrication of biochar from jarul (*Lagerstroemia speciosa*) seed hull for ultrasound aided sequestration of ofloxacin from water: phytotoxic assessments and cost analysis, *J. Mol. Liq.*, 2023, **387**, 122610, DOI: **10.1016/j.molliq.2023.122610**.

23 M. Namakka and R. Rahman, RSC Advances Insights into micro-and nano-zero valent iron materials: synthesis methods and multifaceted applications, *RSC Adv.*, 2024, **14**, 30411–30439, DOI: **10.1039/D4RA03507K**.

24 S. Saravanan, R. S. Dubey, S. Saravanan and R. S. Dubey, Synthesis of SiO_2 Nanoparticles by Sol–Gel Method and Their Optical and Structural Properties Thin films for Opto-Electronic Applications View project Nanomaterials View project Synthesis of SiO_2 Nanoparticles by Sol–Gel Method and Their Optical and Structural Properties, *Romanian J. Inf. Sci. Technol.*, 2020, **23**, 105–112. Available from: **https://www.researchgate.net/publication/338828540**.

25 A. O. Araoyinbo, M. M. A. L. Bakri Abdullah, M. A. Anuar Mohd Salleh, N. N. Abdul Aziz and A. Iskandar Azmi, Phase study of titanium dioxide nanoparticle prepared via sol–gel process, *IOP Conf. Ser.: Mater. Sci. Eng.*, 2018, 343, DOI: **10.1088/1757-899X/343/1/012011**.

26 X. Gao, C. Xu, H. Yin, P. Chen, X. Wang and Q. Song, *et al.*, Synthesis of nano titanium oxide with controlled oxygen content using pulsed discharge in water, *Adv. Powder Technol.*, 2020, **31**(3), 986–992.

27 M. Lal, P. Sharma and C. Ram, Calcination temperature effect on titanium oxide (TiO_2) nanoparticles synthesis, *Optik*, 2021, **241**, 166934, DOI: **10.1016/j.ijleo.2021.166934**.

28 B. Saha, A. Debnath and B. Saha, Fabrication of PANI@Fe–Mn–Zr hybrid material and assessments in sono-assisted adsorption of methyl red dye: uptake performance and response surface optimization, *J. Indian Chem. Soc.*, 2022, **99**(9), 100635, DOI: **10.1016/j.jics.2022.100635**.

29 S. Das, A. Pal and A. Debnath, Polyaniline-Coated Magnesium Ferrite Nanocomposite: Synthesis, Characterization, Fabrication Cost Analysis and Dye Sorption Behavior with Scale-Up Design, *ChemistrySelect*, 2023, **8**(29), 1–13, DOI: **10.1002/slct.202300928**, **www.chemistryselect.org**.

30 Y. Wu, J. W. Bai, J. Y. Zhu, Z. H. Li, Y. F. Shao and Q. Q. Xiao, Unveiling the traits of dry and wet pre-magnetized zero-valent iron-activated peroxymonosulfate: degradation of oxytetracycline, *Chemosphere*, 2023, **344**, 140348, DOI: **10.1016/j.chemosphere.2023.140348**.

31 Z. Ci, Y. Yue, J. Xiao, X. Huang and Y. Sun, Spectroscopic and modeling investigation of U(VI) removal mechanism on nanoscale zero-valent iron/clay composites, *J. Colloid Interface Sci.*, 2023, **630**, 395–403.

32 H. Yang, L. Deng, H. Yang, Y. Xiao and D. Zheng, Promotion of nitrogen removal in a zero-valent iron-mediated nitrogen removal system operated in co-substrate mode, *Chemosphere*, 2022, **307**(P2), 135779, DOI: **10.1016/j.chemosphere.2022.135779**.

33 W. Ma, Z. Cao, X. Shi, S. H. Deng, H. Dai and B. Xie, Synergistic effects of zero-valent iron-carbon galvanic cells on the microalgal-bacterial symbiosis system for efficient anaerobic digestion effluent treatment, *J. Water Process Eng.*, 2023, **56**, 104296, DOI: **10.1016/j.jwpe.2023.104296**.

34 Y. Wu, C. Y. Guan, N. Griswold, L. Y. Hou, X. Fang and A. Hu, *et al.*, Zero-valent iron-based technologies for removal of heavy metal(loid)s and organic pollutants from the aquatic environment: recent advances and perspectives, *J. Cleaner Prod.*, 2020, **277**, 123478, DOI: **10.1016/j.jclepro.2020.123478**.

35 A. M. Zafar, A. Naeem, M. A. Minhas, M. J. Hasan, S. Rafique and A. Ikhlaq, Removal of reactive dyes from textile industrial effluent using electrocoagulation in different parametric conditions of aluminum electrodes, *Total Environ. Adv.*, 2024, **9**, 200087, DOI: **10.1016/j.teadva.2023.200087**.

36 Q. Zhang, D. Zhao, S. Feng, Y. Wang, J. Jin and A. Alsaedi, *et al.*, Synthesis of nanoscale zero-valent iron loaded chitosan for synergistically enhanced removal of U(VI) based on adsorption and reduction, *J. Colloid Interface Sci.*, 2019, **552**, 735–743, DOI: **10.1016/j.jcis.2019.05.109**.

37 Y. Duan, F. Liu, X. Liu and M. Li, Removal of Cr(VI) by glutaraldehyde-crosslinked chitosan encapsulating micro-scale zero-valent iron: synthesis, mechanism, and longevity, *J. Environ. Sci.*, 2023, **142**, 115–128.

38 C. Ratanaphain, D. Viboonratanasri, P. Prompinit, S. Krajangpan, E. Khan and P. Punyapalakul, Mechanistic study of iodoacetamide degradation by functionalized SiO_2-coated nZVI: the role of surface functional groups on adsorption, dehalogenation and hydrolysis, *J. Water Process Eng.*, 2024, **63**, 105485, DOI: **10.1016/j.jwpe.2024.105485**.

39 Z. Hejri, M. Hejri, M. Omidvar and S. Morshedi, Synthesis of TiO_2/nZVI nanocomposite for nitrate removal from aqueous solution, *Int. J. Ind. Chem.*, 2019, **10**(3), 225–236, DOI: **10.1007/s40090-019-0186-3**.

40 M. Kazemi, M. Peyravi and M. Jahanshahi, Multilayer UF membrane assisted by photocatalytic NZVI@TiO_2 nanoparticle for removal and reduction of hexavalent chromium, *J. Water Process Eng.*, 2020, **37**, 101183, DOI: **10.1016/j.jwpe.2020.101183**.

41 J. Feng, G. Lang, T. Li, J. Zhang, T. Li and Z. Jiang, Enhanced removal performance of zero-valent iron towards heavy metal ions by assembling Fe-tannin coating, *J. Environ. Manage.*, 2022, **319**, 115619, DOI: **10.1016/j.jenvman.2022.115619**.

42 X. Man, X. A. Ning, H. Zou, J. Liang, J. Sun and X. Lu, *et al.*, Removal of polycyclic aromatic hydrocarbons (PAHs) from textile dyeing sludge by ultrasound combined zero-valent iron/EDTA/Air system, *Chemosphere*, 2018, **191**, 839–847, DOI: **10.1016/j.chemosphere.2017.10.043**.

43 Y. Song, H. Tang, Y. Yan, Y. Guo, H. Wang and Z. Bian, Combining electrokinetic treatment with modified zero-valent iron nanoparticles for rapid and thorough dechlorination of trichloroethene, *Chemosphere*, 2022, **292**(19), 133443, DOI: **10.1016/j.chemosphere.2021.133443**.

44 Y. X. Song, S. Chen, N. You, H. T. Fan and L. N. Sun, Nanocomposites of zero-valent Iron@Activated carbon derived from corn stalk for adsorptive removal of tetracycline antibiotics, *Chemosphere*, 2020, **255**, 126917, DOI: **10.1016/j.chemosphere.2020.126917**.

45 J. Zeng, J. Liu, W. Su, J. Tang, Z. Luo and F. Tang, *et al.*, Persulfate activation by sulfide-modified nanoscale zero-

valent iron for metronidazole degradation: mechanism, major radicals and toxicity assessment, *J. Water Process Eng.*, 2023, **53**, 103733, DOI: 10.1016/j.jwpe.2023.103733.

46 X. Zhang, Z. Yao, Y. Gao, S. Yan, X. Peng and W. Shen, Efficient Cu(II) removal with boronated zero-valent iron via inhibition of oxygen adsorption and enhanced electron transfer, *Appl. Surf. Sci.*, 2024, **654**, 159466, DOI: 10.1016/j.apsusc.2024.159466.

47 M. M. El-shafei, A. Hamdy and M. M. Hefny, Zero-valent iron nanostructures: synthesis, characterization and application, *J. Environ. Biotechnol. Res.*, 2018, 7(1), 1–10.

48 J. Hou, Y. Li, H. Ci, L. Miao, G. You and J. Wu, *et al.*, Influence of aggregation and sedimentation behavior of bare and modified zero-valent-iron nanoparticles on the Cr(VI) removal under various groundwater chemistry conditions, *Chemosphere*, 2022, **296**, 133905, DOI: 10.1016/j.chemosphere.2022.133905.

49 G. Kozma, A. Rónavári, Z. Kónya and Á. Kukovecz, Environmentally Benign Synthesis Methods of Zero-Valent Iron Nanoparticles, *ACS Sustainable Chem. Eng.*, 2016, **4**(1), 291–297.

50 D. Jiang, D. Huang, C. Lai, P. Xu, G. Zeng and J. Wan, *et al.*, Difunctional chitosan-stabilized Fe/Cu bimetallic nanoparticles for removal of hexavalent chromium wastewater, *Sci. Total Environ.*, 2018, **644**, 1181–1189, DOI: 10.1016/j.scitotenv.2018.06.367.

51 F. S. D. Santos, F. R. Lago, L. Yokoyama and F. V. Fonseca, Synthesis and characterization of zero-valent iron nanoparticles supported on SBA-15, *J. Mater. Res. Technol.*, 2017, **6**(2), 178–183, DOI: 10.1016/j.jmrt.2016.11.004.

52 L. Di, X. Chen, J. Lu, Y. Zhou and Y. Zhou, Removal of heavy metals in water using nano zero-valent iron composites: a review, *J. Water Process Eng.*, 2023, **53**, 103913, DOI: 10.1016/j.jwpe.2023.103913.

53 K. N. Suryakant, H. Tripathi, S. Kumar and S. Bhardwaj, Sol–gel synthesis of Tin oxide nanoparticles and their characterizations, *Mater. Today Proc.*, 2023, DOI: 10.1016/j.matpr.2023.06.072.

54 A. Zielinska, F. Carreiró, A. M. Oliveira, A. Neves, B. Pires and D. Nagasamy Venkatesh, *et al.*, Polymeric Nanoparticles: Production, Characterization, Toxicology and Ecotoxicology, *Molecules*, 2020, **25**, 3731, DOI: 10.3390/molecules25163731.

55 Y. P. Sun, X. Q. Li, J. Cao, W. X. Zhang and H. P. Wang, Characterization of zero-valent iron nanoparticles, *Adv. Colloid Interface Sci.*, 2006, **120**(1–3), 47–56.

56 L. Guo, Amorphous nanomaterials: preparation, characterization and applications.

57 T. Liu, P. Wang and Z. L. Wang, A high-efficient and recyclable aged nanoscale zero-valent iron compound for V^{5+} removal from wastewater: characterization, performance and mechanism, *Chemosphere*, 2022, **302**, 134833, DOI: 10.1016/j.chemosphere.2022.134833.

58 Y. Rashtbari, F. Sher, S. Afshin, A. Hamzezadeh bahrami, S. Ahmadi and O. Azhar, *et al.*, Green synthesis of zero-valent iron nanoparticles and loading effect on activated carbon for furfural adsorption, *Chemosphere*, 2022, **287**(P1), 132114, DOI: 10.1016/j.chemosphere.2021.132114.

59 A. O. Dada, F. A. Adekola, E. O. Odebunmi, F. E. Dada, O. S. Bello and A. S. Ogunlaja, Bottom-up approach synthesis of core–shell nanoscale zerovalent iron (CS-nZVI): physicochemical and spectroscopic characterization with Cu(II) ions adsorption application, *MethodsX*, 2020, **7**, 100976, DOI: 10.1016/j.mex.2020.100976.

60 S. Li, W. Wang, F. Liang and W. X. Zhang, Heavy metal removal using nanoscale zero-valent iron (nZVI): theory and application, *J. Hazard. Mater.*, 2017, **322**, 163–171, DOI: 10.1016/j.jhazmat.2016.01.032.

61 S. N. Zhu, G. H. Liu, K. S. Hui, Z. Ye and K. N. Hui, A facile approach for the synthesis of stable amorphous nanoscale zero-valent iron particles, *Electron. Mater. Lett.*, 2014, **10**(1), 143–146.

62 H. Li, J. Wan, Y. Ma, Y. Wang and M. Huang, Influence of particle size of zero-valent iron and dissolved silica on the reactivity of activated persulfate for degradation of acid orange 7, *Chem. Eng. J.*, 2014, **237**, 487–496, DOI: 10.1016/j.cej.2013.10.035.

63 S. Feng, B. Zhang, J. Wang and J. Jeanne, Zero-valent iron in phosphate removal: unraveling the role of particle size and dissolved oxygen, *J. Water Process Eng.*, 2024, **60**, 105180, DOI: 10.1016/j.jwpe.2024.105180.

64 J. Liu, A. Liu, J. Guo, T. Zhou and W. X. Zhang, Enhanced aggregation and sedimentation of nanoscale zero-valent iron (nZVI) with polyacrylamide modification, *Chemosphere*, 2021, **263**, 127875, DOI: 10.1016/j.chemosphere.2020.127875.

65 D. Jiang, X. Hu, R. Wang and D. Yin, Oxidation of nanoscale zero-valent iron under sufficient and limited dissolved oxygen: influences on aggregation behaviors, *Chemosphere*, 2015, **122**, 8–13, DOI: 10.1016/j.chemosphere.2014.09.095.

66 S. Xie, J. Su, J. Zhao, H. Yang and H. Qian, An amorphous zero-valent iron decorated by Fe_3O_4 significantly improves the Fenton-like reaction, *J. Alloys Compd.*, 2022, **929**, 167306, DOI: 10.1016/j.jallcom.2022.167306.

67 Y. Zhang, X. Gao and C. Xu, The sequestration of Cr(VI) by zero valent iron under a non-uniform magnetic field: an interfacial dynamic reaction, *Chemosphere*, 2020, **249**, 126057, DOI: 10.1016/j.chemosphere.2020.126057.

68 Q. Ma, H. Zhang, X. Deng, Y. Cui, X. Cheng and X. Li, *et al.*, Electrochemical fabrication of NZVI/TiO_2 nano-tube arrays photoelectrode and its enhanced visible light photocatalytic performance and mechanism for degradation of 4-chlorphenol, *Sep. Purif. Technol.*, 2017, **182**, 144–150.

69 X. Wang, P. Huang, P. Zhang, C. Wang, F. He and H. Sun, Synthesis of stabilized zero-valent iron particles and role investigation of humic acid-Fex + shell in Fenton-like reactions and surface stability control, *J. Hazard. Mater.*, 2024, **465**, 133296, DOI: 10.1016/j.jhazmat.2023.133296.

70 Z. Liu, G. Chen, F. Hu and X. Li, Synthesis of mesoporous magnetic $MnFe_2O_4$@CS-SiO_2 microsphere and its adsorption performance of Zn^{2+} and MB studies, *J. Environ. Manage.*, 2020, **263**, 110377, DOI: 10.1016/j.jenvman.2020.110377.

71 X. Zhang, W. Sun, Y. Wang, Z. Li, X. Huang and T. Li, *et al.*, Mechanochemical synthesis of microscale zero-valent iron/N-doped graphene-like biochar composite for degradation of tetracycline via molecular O_2 activation, *J. Colloid Interface Sci.*, 2024, **659**, 1015–1028, DOI: 10.1016/j.jcis.2024.01.061.

72 M. Jaroniec, M. Kruk and A. Sayari, Adsorption methods for characterization of surface and structural properties of mesoporous molecular sieves, *Stud. Surf. Sci. Catal.*, 1998, **117**, 325–332, DOI: 10.1016/S0167-2991(98)81008-2.

73 J. Xu, X. Zhang, C. Sun, H. He, Y. Dai and S. Yang, *et al.*, Catalytic degradation of diatrizoate by persulfate activation with peanut shell biochar-supported nano zero-valent iron in aqueous solution, *Int. J. Environ. Res. Public Health*, 2018, **15**(9), 1–18.

74 A. Balakrishnan and M. Chinthala, Comprehensive review on advanced reusability of g-C_3N_4 based photocatalysts for the removal of organic pollutants, *Chemosphere*, 2022, **297**, 134190, DOI: 10.1016/j.chemosphere.2022.134190.

75 J. H. Won, M. K. Kim, H. S. Oh and H. M. Jeong, Scalable production of visible light photocatalysts with extended nanojunctions of WO_3/g-C_3N_4 using zeta potential and phase control in sol–gel process, *Appl. Surf. Sci.*, 2023, **612**, 155838, DOI: 10.1016/j.apsusc.2022.155838.

76 J. Fan, Y. Guo, J. Wang and M. Fan, Rapid decolorization of azo dye methyl orange in aqueous solution by nanoscale zerovalent iron particles, *J. Hazard. Mater.*, 2009, **166**(2–3), 904–910.

77 M. Suzuki, Y. Suzuki, K. Uzuka and Y. Kawase, Biological treatment of non-biodegradable azo-dye enhanced by zero-valent iron (ZVI) pre-treatment, *Chemosphere*, 2020, **259**, 127470, DOI: 10.1016/j.chemosphere.2020.127470.

78 G. Zamiri, A. S. M. A. Haseeb, P. Jagadish, M. Khalid, I. Kong and S. G. Krishnan, Three-Dimensional Graphene-TiO_2-SnO_2Ternary Nanocomposites for High-Performance Asymmetric Supercapacitors, *ACS Omega*, 2022, **7**(48), 43981–43991.

79 G. Zhang, F. Yang, W. Yang and Y. Li, N-doped carbon nanotube encapsulated nZVI as a high-performance bifunctional catalyst for oxidative desulfurization, *Particuology*, 2023, **81**, 109–118, DOI: 10.1016/j.partic.2023.01.002.

80 D. I. Anwar and D. Mulyadi, Synthesis of Fe–TiO_2 Composite as a Photocatalyst for Degradation of Methylene Blue, *Proc. Chem.*, 2015, **17**, 49–54, DOI: 10.1016/j.proche.2015.12.131.

81 Y. Huang, W. Zhang, M. Zhang, X. Zhang and Y. Zhao, Hydroxyl-functionalized TiO_2@SiO_2@Ni/nZVI nanocomposites fabrication, characterization and enhanced simultaneous visible light photocatalytic oxidation and adsorption of arsenite, *Chem. Eng. J.*, 2018, **338**, 369–382.

82 S. Madan, R. Shaw, S. Tiwari and S. K. Tiwari, Enhancing corrosion stability and shelf life of nanoscale zero-valent iron via encapsulation in porous Ze–TiO_2 matrix: an interface for simultaneous oxidation and adsorption of As(III), *Colloids Surf., A*, 2020, **607**, 125381, DOI: 10.1016/j.colsurfa.2020.125381.

83 V. B. Mbayachi, E. Ndayiragije, T. Sammani, S. Taj, E. R. Mbuta and A. U. Khan, Graphene synthesis, characterization and its applications: a review, *Results Chem.*, 2021, **3**, 100163, DOI: 10.1016/j.rechem.2021.100163.

84 D. Ding, Y. Zhao, Y. Chen, C. Xu, X. Fan and Y. Tu, *et al.*, Recent advances in bimetallic nanoscale zero-valent iron composite for water decontamination: synthesis, modification and mechanisms, *J. Environ. Manage.*, 2024, **353**, 120187, DOI: 10.1016/j.jenvman.2024.120187.

85 A. Pavelková, V. Cencerová, J. Zeman, V. Antos and J. Nosek, Reduction of chlorinated hydrocarbons using nano zero-valent iron supported with an electric field. Characterization of electrochemical processes and thermodynamic stability, *Chemosphere*, 2021, **265**, 128764, DOI: 10.1016/j.chemosphere.2020.128764.

86 Y. Quintero, E. Mosquera, J. Diosa and A. García, Ultrasonic-assisted sol–gel synthesis of TiO_2 nanostructures: influence of synthesis parameters on morphology, crystallinity, and photocatalytic performance, *J. Sol-Gel Sci. Technol.*, 2020, **94**(2), 477–485.

87 L. Wang, Y. Li, R. Zou, R. Sun, H. Tian and G. Luo, *et al.*, Insight into the influence of environmental factors on selenite removal from desulfurization wastewater by NZVI@AC: an experimental and theoretical study, *J. Water Process Eng.*, 2024, **57**, 104674, DOI: 10.1016/j.jwpe.2023.104674.

88 X. Guan, Y. Sun, H. Qin, J. Li, I. M. C. Lo and D. He, *et al.*, The limitations of applying zero-valent iron technology in contaminants sequestration and the corresponding countermeasures: the development in zero-valent iron technology in the last two decades (1994–2014), *Water Res.*, 2015, **75**, 224–248.

89 R. Zhang, R. Napolano, B. Xi, A. M. Salazar, Q. Shi and Y. Zhao, *et al.*, Mechanistic insights into Cr(VI) removal by a combination of zero-valent iron and pyrite, *Chemosphere*, 2023, **330**, 138693, DOI: 10.1016/j.chemosphere.2023.138693.

90 H. Qin, X. Guan, J. Z. Bandstra, R. L. Johnson and P. G. Tratnyek, Modeling the Kinetics of Hydrogen Formation by Zerovalent Iron: Effects of Sulfidation on Micro- and Nano-Scale Particles, *Environ. Sci. Technol.*, 2018, **52**(23), 13887–13896.

91 X. Ling, J. Li, W. Zhu, Y. Zhu, X. Sun and J. Shen, *et al.*, Synthesis of nanoscale zero-valent iron/ordered mesoporous carbon for adsorption and synergistic reduction of nitrobenzene, *Chemosphere*, 2012, **87**(6), 655–660, DOI: 10.1016/j.chemosphere.2012.02.002.

92 L. Chen, S. Feng, D. Zhao, S. Chen, F. Li and C. Chen, Efficient sorption and reduction of U(VI) on zero-valent iron-polyaniline-graphene aerogel ternary composite, *J. Colloid Interface Sci.*, 2017, **490**, 197–206, DOI: 10.1016/j.jcis.2016.11.050.

93 R. Garg, M. Mittal, S. Tripathi and N. O. Eddy, Core to concept: synthesis, structure, and reactivity of nanoscale zero-valent iron (NZVI) for wastewater remediation, *Environ. Sci. Pollut. Res.*, 2024, 0123456789, DOI: 10.1007/s11356-024-33197-x.

94 N. Fujioka, M. Suzuki, S. Kurosu and Y. Kawase, Linkage of iron elution and dissolved oxygen consumption with

removal of organic pollutants by nanoscale zero-valent iron: effects of pH on iron dissolution and formation of iron oxide/hydroxide layer, *Chemosphere*, 2016, **144**, 1738–1746, DOI: 10.1016/j.chemosphere.2015.10.064.

95 P. Das and A. Debnath, Fabrication of $MgFe_2O_4$/polyaniline nanocomposite for amputation of methyl red dye from water: isotherm modeling, kinetic and cost analysis, *J. Dispersion Sci. Technol.*, 2023, **44**(14), 2587–2598, DOI: 10.1080/01932691.2022.2110110.

96 S. Das, S. R. Paul and A. Debnath, Enhanced performance of *Lagerstroemia speciosa* seed biochar and polypyrrole composite for the sequestration of emerging contaminant from wastewater sample: case study of ofloxacin drug, *J. Water Process Eng.*, 2024, **64**, 105699, DOI: 10.1016/j.jwpe.2024.105699.

97 D. F. F. Brossault, T. M. McCoy and A. F. Routh, Self-assembly of $TiO_2/Fe_3O_4/SiO_2$ microbeads: a green approach to produce magnetic photocatalysts, *J. Colloid Interface Sci.*, 2021, **584**, 779–788.

98 Í. Lacerda Fernandes, D. Pereira Barbosa, S. Botelho de Oliveira, V. Antônio da Silva, M. Henrique Sousa and M. Montero-Muñoz, *et al.*, Synthesis and characterization of the MNP@SiO_2@TiO_2 nanocomposite showing strong photocatalytic activity against methylene blue dye, *Appl. Surf. Sci.*, 2022, **580**, 152195, DOI: 10.1016/j.apsusc.2021.152195.

99 H. H. Mungondori, S. Ramujana, D. M. Katwire and R. T. Taziwa, Synthesis of a novel visible light responsive γ-Fe_2O_3/SiO_2/C-TiO_2 magnetic nanocomposite for water treatment, *Water Sci. Technol.*, 2018, **78**(12), 2500–2510.

100 D. Chen, Y. Chen, Y. Li and S. Ye, Preparation and photocatalytic properties of a visible light responsive and magnetically separated photocatalyst of γ-Fe_2O_3/SiO_2/GSs/TiO_2, *Micro Nano Lett.*, 2015, **10**(5), 267–271.

101 Y. Lu, M. Feng and Y. Wang, Enhancing the heterogeneous electro-Fenton degradation of methylene blue using sludge-derived biochar-loaded nano zero-valent iron, *J. Water Process Eng.*, 2024, **59**, 104980, DOI: 10.1016/j.jwpe.2024.104980.

102 A. K. Inamdar, N. R. Hulsure, A. S. Kadam, R. S. Rajenimbalkar, R. Karpoormath and S. B. Shelke, *et al.*, Flame synthesized tetragonal TiO_2 nanoparticles for Methylene Blue and Congo Red dye removal applications, *Results Chem.*, 2023, **5**, 100854, DOI: 10.1016/j.rechem.2023.100854.

103 J. R. Rajabathar, R. Thankappan, A. Sutha, H. Al-Lohedan, A. Mahmoud Karami and S. Ashok Kumar, *et al.*, Enhanced photocatalytic activity of magnetite/titanate (Fe_3O_4/TiO_2) nanocomposite for methylene blue dye degradation under direct sunlight, *Opt. Mater.*, 2024, **148**, 114820, DOI: 10.1016/j.optmat.2023.114820.

104 T. Takele, K. Angassa, M. Abewaa, A. M. Kebede and I. Tessema, Adsorption of methylene blue from textile industrial wastewater using activated carbon developed from H_3PO_4-activated khat stem waste, *Biomass Convers. Biorefin.*, 2023, DOI: 10.1007/s13399-023-05245-y.

105 X. Sun, T. Kurokawa, M. Suzuki, M. Takagi and Y. Kawase, Removal of cationic dye methylene blue by zero-valent iron: effects of pH and dissolved oxygen on removal mechanisms, *J. Environ. Sci. Health, Part A: Toxic/Hazard. Subst. Environ. Eng.*, 2015, **50**(10), 1057–1071.

106 M. Bahrami, M. J. Amiri, S. Rajabi and M. Mahmoudi, The removal of methylene blue from aqueous solutions by polyethylene microplastics: modeling batch adsorption using random forest regression, *Alexandria Eng. J.*, 2024, **95**, 101–113, DOI: 10.1016/j.aej.2024.03.100.

107 E. Petala, M. Baikousi, M. A. Karakassides, G. Zoppellaro, J. Filip and J. Tuček, *et al.*, Synthesis, physical properties and application of the zero-valent iron/titanium dioxide heterocomposite having high activity for the sustainable photocatalytic removal of hexavalent chromium in water, *Phys. Chem. Chem. Phys.*, 2016, **18**(15), 10637–10646.

108 M. Zhao, Z. Niu, Y. Xu, F. Fan, W. Wu and D. Pan, One-step electrospinning preparation of magnetic NZVI@TiO_2 nanofibers for enhanced immobilization of U(VI) from aqueous solution, *J. Radioanal. Nucl. Chem.*, 2023, **332**(4), 1083–1091.

109 T. Zeng, H. Nong, H. Sha, S. Chen, X. Zhang and J. Liu, Performance and mechanism of Cr(VI) removal by sludge-derived biochar loaded with nanoscale zero-valent iron, *Fuhe Cailiao Xuebao*, 2023, **40**(2), 1037–1049, DOI: 10.1016/j.dwt.2024.100035.

110 D. Xu, S. Zheng, T. Sun, G. Gao, Y. Sun and H. Jia, *et al.*, Simultaneous adsorption and reduction of Cr(VI) on Potamogeton·crispus biochar supported nanoscale zero-valent iron: electro- and sepctro-chemical mechanism, *J. Taiwan Inst. Chem. Eng.*, 2024, **155**, 105259, DOI: 10.1016/j.jtice.2023.105259.

111 T. He, J. Q. Hua, R. P. Chen and L. Yu, Adsorption characteristics of methylene blue by a dye-degrading and extracellular polymeric substance-producing strain, *J. Environ. Manage.*, 2021, **288**, 112446, DOI: 10.1016/j.jenvman.2021.112446.

112 M. Kobayashi, Y. Maeda, T. Hoshi, J. Okubo and Y. Tanizaki, Analysis of the electronic absorption spectrum of adsorbed layers of methylene blue, *J. Soc. Dyers Colour.*, 1989, **105**(10), 362–368.

113 J. J. Salazar-Rabago, R. Leyva-Ramos, J. Rivera-Utrilla, R. Ocampo-Perez and F. J. Cerino-Cordova, Biosorption mechanism of Methylene Blue from aqueous solution onto White Pine (*Pinus durangensis*) sawdust: effect of operating conditions, *Sustainable Environ. Res.*, 2017, **27**(1), 32–40, DOI: 10.1016/j.serj.2016.11.009.

114 D. W. Elliott and W. X. Zhang, Field assessment of nanoscale bimetallic particles for groundwater treatment, *Environ. Sci. Technol.*, 2001, **35**(24), 4922–4926.

115 B. Karn, T. Kuiken and M. Otto, Nanotechnology and in situ remediation: a review of the benefits and potential risks, *Environ. Health Perspect.*, 2009, **117**(12), 1823–1831.

116 T. Das, A. Debnath and M. S. Manna, Adsorption of malachite green by Aegle marmelos-derived activated biochar: novelty assessment through phytotoxicity tests and economic analysis, *J. Indian Chem. Soc.*, 2024, **101**(9), 101219, DOI: 10.1016/j.jics.2024.101219.

117 B. Saha, A. Debnath and B. Saha, Polypyrrole-encapsulated metal oxide nanocomposite for adsorptive abatement of anionic dye from dye laden wastewater: cost analysis and scale up design, *Mater. Today Commun.*, 2024, **39**, 109061, DOI: 10.1016/j.mtcomm.2024.109061.